Snow water equivalent estimates from airborne radar in the St. Elias Mountains

Journal:	*Journal of Glaciology*
Manuscript ID	Draft
Manuscript Type:	Article
Date Submitted by the Author:	n/a
Complete List of Authors:	Daniel, Michael; The University of Arizona Department of Planetary Sciences and Lunar and Planetary Laboratory Holt, John; The University of Arizona Department of Planetary Sciences and Lunar and Planetary Laboratory; The University of Arizona Department of Geosciences Mannello, Mikaila; The University of Maine Climate Change Institute; The University of Maine, Department of Earth and Climate Sciences Li, Jilu; The University of Kansas, The Center for Remote Sensing and Integrated Systems Rodriguez-Morales, Fernando; University of Kansas, The Center for Remote Sensing and Integrated Systems Brinkerhoff, Douglas; University of Montana, Department of Computer Science Truffer, Martin; University of Alaska Fairbanks Geophysical Institute; University of Alaska Fairbanks, Department of Physics
Keywords:	Ground-penetrating radar, Accumulation, Remote sensing, Snow
Abstract:	Quantifying the input mass from snow accumulation on rapidly changing glaciers is critical to establishing baseline states and predicting responses to climate change. Some of the largest glaciers in the world are located in the St. Elias Mountains in Southeast Alaska and Southwest Yukon; however, the input mass to these glaciers is poorly constrained. Here we used airborne radar sounding combined with in situ measurements of snow properties, and satellite imagery from Landsat 8/9 and Sentinel 1,

	to estimate the winter mass balance on the Bering, Hubbard, Kaskawulsh, Logan, Seward, Walsh, and Yahtse glaciers. Along-track snow water equivalent measurements for the winter accumulation period range from 0 to 3 m in 2018, 0.2 to 3.4 m in 2021, and 1.1 to 3.3 m in 2023. On-glacier measurements from the Seward and Kaskawulsh glaciers provided a mean seasonal snow density of 438 ± 22 kg m^{-3} which leads to a real dielectric permittivity of 1.86 ± 0.12, similar to values from other Alaskan glaciers. We observed that the maritime glaciers Yahtse, Bering, Hubbard, and Seward receive significantly more accumulation than the more inland glaciers

Snow water equivalent estimates from airborne radar in the St. Elias Mountains

Michael F. Daniel[1], John W. Holt[1,2], Mikaila Mannello[3,4], Jilu Li[5], Fernando Rodriguez-Morales[5], Douglas J. Brinkerhoff[6], Martin Truffer[7,8]

[1]*Lunar and Planetary Laboratory, University of Arizona, Tucson, AZ, USA*

[2]*Department of Geosciences, University of Arizona, Tucson, AZ, USA*

[3]*Climate Change Institute, University of Maine, Orono, ME, USA*

[4]*Department of Earth and Climate Sciences, University of Maine, Orono, ME, USA*

[5]*The Center for Remote Sensing and Integrated Systems, University of Kansas, Lawrence, KS, USA*

[6]*Department of Computer Science, University of Montana, Missoula, MT, USA*

[7]*Geophysical Institute, University of Alaska Fairbanks, Fairbanks, AK, USA* [8]*Department of Physics, University of Alaska Fairbanks, Fairbanks, AK, USA*

Correspondence: Michael Daniel <mfdaniel@arizona.edu>

ABSTRACT. Quantifying the input mass from snow accumulation on rapidly changing glaciers is critical to establishing baseline states and predicting responses to climate change. Some of the largest glaciers in the world are located in the St. Elias Mountains in Southeast Alaska and Southwest Yukon; however, the input mass to these glaciers is poorly constrained. Here we used airborne radar sounding combined with in situ measurements of snow properties, and satellite imagery from Landsat 8/9 and Sentinel 1, to estimate the winter mass balance on the Bering, Hubbard, Kaskawulsh, Logan, Seward, Walsh, and Yahtse glaciers. Along-track snow water equivalent measurements for the winter accumulation period range from 0 to 3 m in 2018, 0.2 to 3.4 m in 2021, and 1.1 to 3.3 m in 2023. On-glacier measurements from the Seward and Kaskawulsh glaciers provided a mean seasonal snow density of 438 $\pm$ 22 kg m^{-3} which leads to a real dielectric permittivity of 1.86 $\pm$ 0.12, similar to values from other Alaskan glaciers. We observed that the maritime glaciers

Yahtse, Bering, Hubbard, and Seward receive significantly more accumulation than the more inland glaciers.

1 INTRODUCTION

The most commonly used indicator of glacier health is mass balance, which is the difference between mass gain (primarily snowfall) and mass loss (primarily surface melt and/or calving) over a period (Cogley and others, 2011). Successive years of negative mass balance are the sign of a retreating glacier. Although the mass balance for Alaskan glaciers has some constraints from long-term repeat altimetry measurements that show a thinning of most glaciers (Larsen and others, 2015), the individual mass loss and gain terms are not well constrained. Complicating input mass retrieval is that measuring snowfall in mountainous terrain is currently one of the most challenging problems in snow hydrology (Dozier and others, 2016). It has already been observed that snow accumulation patterns in Alaska have been changing since the onset of industrialization (Winski and others, 2017). Thus, determining baseline mass accumulation rates for glaciers is critical for defining their current states and predicting responses to climate change.

The Randolph Glacier Inventory (RGI) Region 1, called Alaska, includes glaciers in Alaska, Southwest Yukon, and Western British Columbia. RGI Region 1 contains 13% of the world's glacial ice, excluding the Greenland and Antarctica ice sheets but including their peripheral glaciers (Millan and others, 2022). For 2000-2019, RGI Region 1 was the largest non-ice sheet contributor to global sea level rise (Hugonnet and others, 2021) and is expected to continue being a key source through 2100 (Rounce and others, 2023). Our study focuses on seven glaciers in the heavily glaciated St. Elias Mountains of Southeast Alaska and Southwest Yukon (Fig. 1): Bering, Hubbard, Kaskawulsh, Logan, Seward, Walsh, and Yahtse. We use the convention of Seward to include both the Seward and Sít' Tlein (Malaspina) Glaciers, as Seward is the accumulation area for Sít' Tlein and shares a RGI shape file. These seven glaciers cover 15% of the total RGI Region 1 glacier surface area (RGI Consortium, 2023) and have ice coverage from sea level to 5959 m a.s.l. at the summit of Mt. Logan (Fig. S1) (OpenTopography, 2021). Also of note is that Seward, Bering, and Hubbard are among the ten largest glaciers in the world (Windnagel and others, 2023), yet there are very few contraints on the total accumulation for these major glaciers.

In situ measurements (i.e. snow pits and cores) on glacier surfaces are critical to constrain snow density, radar wave velocities, and interpretations of ground penetrating radar (GPR) data, but are generally

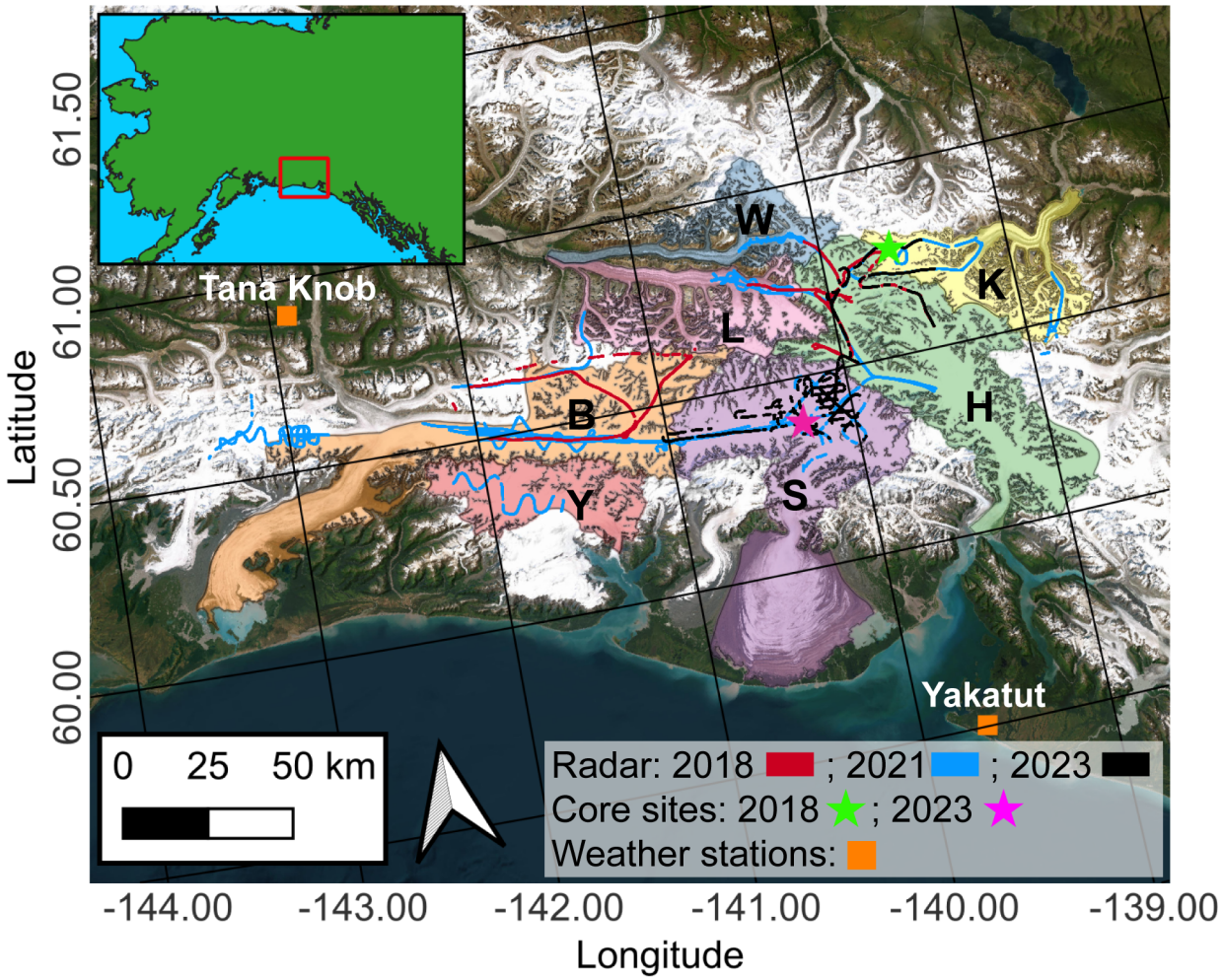

Fig. 1. Airborne radar data coverage, in situ measurement locations, and long-term weather station locations. Glacier outlines are from the Randolph Glacier Inventory v7 (RGI Consortium, 2023). Glaciers are labeled by their first letter; B: Bering, H: Hubbard, K: Kaskawulsh, L: Logan, S: Seward, W: Walsh, and Y: Yahtse. The 2018 core site (green) is from Ochwat and others (2021) and the 2023 core site (magenta) is from our work. This map, and all others in this work, are projected to NAD83/Alaska Albers EPSG:3338.

very sparse (McGrath and others, 2015; Zeller and others, 2022). There are only a few Snow Telemetry (SNOTEL) sites in Southeast Alaska (U.S. Department of Agriculture, 2025), and as these stations are not located to monitor glacier accumulation they are only found off-glacier at low elevations. Where in situ measurements are sparse, end-of-winter GPR surveys are commonly used to measure seasonal snow accumulation on glaciers by detecting the last summer surface (Gusmeroli and others, 2014; McGrath and others, 2015; Li and others, 2023). Snow accumulation for Alaskan glaciers generally occurs from the beginning of October to the end of May (McGrath and others, 2018), with variations due to elevation and local climate.

Li and others (2023) reported snow depths from the St. Elias Mountains in May 2018 and 2021 from airborne frequency modulated continuous wave (FMCW) radar (henceforth airborne radar) with a focus on comparing the snow stratigraphy with a snow/ice core at Mount Wrangell. Due to a lack of in situ measurements, they used a real part of the dielectric permittivity (real permittivity, ϵ') of 1.89 ($v = 0.218$ m ns^{-1}) derived from Alaskan glaciers outside of the St. Elias Mountains (McGrath and others, 2015). A real permittivity of $1.5 - 2$ ($v = 0.245 - 0.212$ m ns^{-1}) is generally accepted for snow (Wu and Liu, 2012) and is related to the radar wave speed through $v = c/\sqrt{\epsilon'}$ where v is the radar wave speed in the material and c is the speed of light in a vacuum. In situ methods for retrieving the real permittivity include hyperbolic analysis (Ni and others, 2010) and empirical relationships between snow density and real permittivity (Sugiyama and others, 2010). Additionally, while Li and others (2023) reported along-track snow depths and snow water equivalent (SWE), their paper's scope did not include winter mass balance estimates. SWE has units of meters water equivalent (m w.e.), and is the equivalent water depth for a column of snow. It is calculated by multiplying the snow depth by the bulk density ratio of snow and water (Beaudoin-Galaise and Jutras, 2022).

Here we estimate the accumulation area winter mass balance in both units of glacier average SWE and mass of water for each the Bering, Hubbard, Kaskawulsh, Seward, Walsh, and Yahtse glaciers for 2018, 2021, and 2023. This is achieved through a combination of airborne radar, in situ measurements, surface-coupled GPR (henceforth surface GPR), and satellite imagery. We used processed airborne radar data collected in 2018 and 2021 as part of NASA's Operation IceBridge (Li and others, 2023; MacGregor and others, 2021), and a new dataset from 2023 using the same radar system on a different aircraft. In situ measurements of snow density from 2018 and 2023 were used to determine the radar wave speed and to convert from snow depth to SWE. This radar wave speed was used to convert the last summer surface

time delay measured by the radar to physical snow depth. Verification of the airborne radar stratigraphy is completed from comparison to surface GPR collected in 2023 on the Seward Glacier. Accumulation areas for each glacier are determined using end-of-summer snow lines digitized from Landsat 8/9 imagery. We also conducted an analysis of Sentinel 1 radar reflectivity to better understand surface melt and how it impacts the airborne radar penetration and airborne radar stratigraphy.

2 DATA SETS AND ANALYSIS METHODS

We first discuss the methods of airborne radar data collection and interpretations followed by the estimates of accumulation area winter mass balance in units of glacier average SWE and mass of water. These estimates are calculated using the input mass to the accumulation area of each glacier. Next, we discuss the methods used for snow density measurement and surface GPR measurements. Lastly, we discuss the determination of equilibrium line altitudes (Landsat 8/9), and surface melt from satellites and weather stations. We discuss the airborne radar first to emphasize that work, though the methods and results from the other data sources are key to the airborne interpretations.

2.1 Airborne radar data

This study used three frequency modulated continuous wave (FMCW) airborne radar datasets. The first two were collected using a radar-equipped Single Otter aircraft from May 20 to 30, 2018 and May 2 to 13, 2021 as part of NASA's Operation IceBridge (Li and others, 2023; MacGregor and others, 2021). These datasets are accessible from the National Snow and Ice Data Center (Paden and others, 2014). The third dataset was collected from May 23 to 24, 2023 using a Cessna 206 aircraft with the radar electronics placed inside its main cabin and with a different antenna configuration compared to what was used in 2018 and 2021. For 2023, The transmit antenna was a high-gain horn (Steatite Qpar QWH-SL-2-18-S-HG-R) mounted on a nadir port available in the aircraft. The receive antenna was a smaller horn (A-info LB-20180-SF) enclosed in a fiber glass fairing, which was attached to the wing-strut (port side) as done priorly on a Cessna 172 (Rodriguez-Morales and others, 2021). The overall antenna feed cable run used in this configuration was shorter, which resulted in ∼1 dB higher received power than previous years. The different antenna configuration in 2023 compared to 2018 and 2023 did not significantly change the airborne radar performance. The airborne radar operated over a frequency range of 2–8 GHz (2018) and 2–6 GHz (2021, 2023), with respective vertical resolution in free space of 2.5 cm and 3.75 cm (Li and others, 2023).

The along-track resolution for the three datasets were ∼1.3 m (Li and others, 2023).

For 2023, the radar waveform deconvolution was derived from specular echoes acquired from the smooth surface of Malaspina Lake at the toe of Seward Glacier. The snow surface was determined from the peak of the deconvolved waveform. Detailed descriptions of the radar development, general configuration, and data processing are discussed in existing publications (Li and others, 2019, 2023; Rodriguez-Morales and others, 2021). The 2023 radar data were processed using the same steps as the 2018 and 2021 data.

The Radar Analysis Graphical Utility (Tober and Christoffersen, 2023), an open source Python tool, was used for all airborne data interpretations. We manually interpreted the top of the first prominent reflector below the surface reflection, representing the previous summer's surface. Where context from snow cores, continuous reflectors, and crossing survey lines exist, we incorporate these constraints to our last summer surface interpretations. Based on data from cores, this can result in the last summer surface corresponding to a reflector below the first prominent subsurface reflector. Where needed, we reinterpret the last summer surface to match with core data. The two-way travel time was converted to snow depth using a constant real permittivity across the region of study following Li and others (2023).

2.1.1 Crossover analysis of snow depth

To validate that interpretations were consistent, we compared intersecting ("crossover") radar tracks to verify that the same reflector was selected in both radargrams. We used a horizontal threshold distance of 50 m for when a crossover occurs and found the difference between the two closest points (Tober and others, 2023). Crossover values were calculated for both physical depth difference and relative difference. The relative difference was used to remove potential biases that could occur when comparing the crossover results between areas of high and low snow thickness. We defined the relative difference as 100 times the absolute difference between the two interpretation depths, divided by the shallower depth. The mean of all crossover points from each year was used as a constraint on the uncertainty of the radar interpretations. Additionally, we performed a crossover analysis between the 2023 surface GPR and airborne radar to analyze differences between the two systems.

2.1.2 Comparing interpreted depths

Another mechanism of validating our interpretations was through comparison with those previously published by Li and others (2023) for 2018 and 2021. Locations with differing interpretations between unique

interpreters are indicative that those areas need additional analysis to infer the last summer surface. We calculated the relative thickness difference between each of the picks from Li and others (2023) to the nearest point in our analysis. By our convention, negative values correspond to our study having deeper (i.e. thicker snow layer) interpretations than those of Li and others (2023). As Li and others (2023) reported snow thickness, not two-way travel time, we recalculated the snow depth using the same real permittivity of 1.89 to facilitate direct comparisons with their interpretations. All other airborne radar and surface GPR comparisons in our work use a real permittivity 1.86 which is calculated in our work from snow density measurements (Sections 2.2.3 and 3.2.3).

2.1.3 Comparison to cores

Once a consistent airborne radar interpretation set was generated, those near the 2018 and 2023 cores were compared to the in situ snow depths. The 2018 cores acquired by Ochwat and others (2021) were located 2.4 km from the nearest 2018 radar data. The 2023 cores were located along or up to approximately 200 meters from the 2021 and 2023 airborne survey lines (Fig. 2). These are the same cores that were used for snow densities measurements and estimating the radar wave speed (Sections 2.2.1 and 3.2.1).

2.1.4 Glacier average SWE and mass estimates

For estimating the accumulation area winter mass balance we constrained the SWE values derived from airborne radar to only those above the ELA. Due to most ice in the St. Elias Mountains being temperate, we assume that all snow falling below the ELA would completely ablate during the summer and won't refreeze (Cuffey and Paterson, 2010; Tober and others, 2023) and therefore do not account for it in our estimates (also due to a lack of data below ELAs).

We first calculated the along-track SWE by multiplying snow depth by the ratio of the column-average snow density to liquid water. Then, for each surface elevation bin above the equilibrium line altitude (ELA), the mean SWE was calculated from all airborne radar interpretations within that elevation bin range. If an elevation bin between the highest and lowest surface elevations with radar measurements was missing data, we linearly interpolated between the two nearest bins with values. We then multiplied the mean SWE at each elevation bin by the fraction of the glacier area at that elevation bin. Next, we sum all elevations bins with data together. To account for the non-sampled part of the accumulation area, we assumed that the previously calculated mean SWE was representative of the non-sampled area and

multiplied it by a factor of one over the fraction of the accumulation area sampled. The resulting value is the winter mass balance glacier average SWE. Hypsometry data from the Randolph Glacier Inventory v7 (RGI Consortium, 2023) was used for the area of each elevation bin and the total glacier area.

As a sensitivity test, we performed a linear interpolation for each glacier from the highest surface elevation bin with airborne radar data to core measurements acquired from Mt. Logan in the early 2000's at King Col (4135 m a.s.l., 0.917 m w.e.) and Prospector Russel Col (PRCol) (5350 m a.s.l., 0.596 m w.e.) (Fisher and others, 2006). While the measurements by Fisher and others (2006) are prior to our data collection, they represent the the only high elevation accumulation measurements currently available for Mt. Logan. As our airborne radar surveys did not reach the highest surface elevations, this sensitivity test investigates the importance of high elevation regions where accumulation is expected to decrease. This test also results in an increase in glacier area being sampled due to the interpolation across the high elevation regions of each glacier.

To convert from SWE to the mass of water, we first estimated the mass from the sampled elevation by summing the elevation bin SWE values multiplied by the bin area, and then converted from units of m w.e. m^{-2} to gigatons of water using the density of water. To account for the area of each glacier not sampled by the airborne radar surveys, we assumed the sampled mass was representative of the non-sampled area and multiplied it by a factor of one over the fraction of the accumulation area sampled. As we do not calculate the summer ablation in this study, our winter mass balance estimates are the maximum possible input mass for each glacier. Additional work should be done to incorporate our winter mass balance estimations with melt models to refine the annual mass balance.

2.2 In situ and surface-coupled measurements

In situ and surface-coupled measurements were collected on the Seward Glacier between May 14 and 22, 2023 (magenta star in Fig. 1) and are shown in further detail in Fig. 2 and Table S1. Snow density, hyperbolic analysis surveys, and common offset radar data were acquired with the primary motivation to support the 2023 airborne data. Cores were acquired around 1650 m a.s.l. Surface GPR sampled the elevation range of 1600 to 1700 m a.s.l. Snow densities from the Seward Glacier are supplemented by two cores drilled 60 cm apart on the Kaskawulsh Glacier (green star in Fig. 1) between May 20 and 24, 2018 at 2640 m a.s.l. (Ochwat and others, 2021).

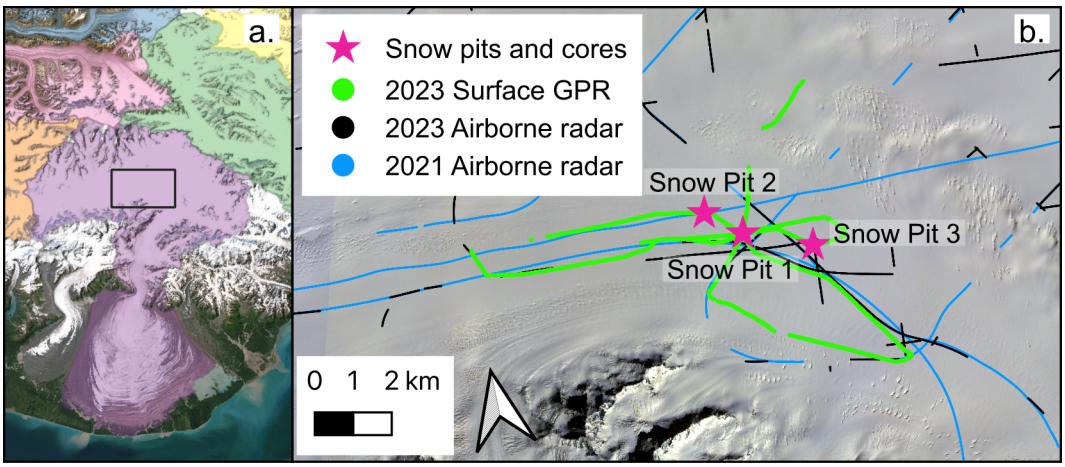

Fig. 2. (a) Seward Glacier with the black box showing the area of panel (b). (b) In situ measurement locations on the Seward Glacier from 2023 shown with the 2023 surface GPR lines and nearby 2021 and 2023 airborne lines. Hyperbolic analysis surveys were collected at Snow Pit 1 (1 m and 1.5 m deep probe) and Snow Pit 3 (1.2 m deep probe).

2.2.1 Snow density

Snow density measurements were acquired on the Seward Glacier on May 15 and 17, 2023. These measurements were taken one week prior to the 2023 airborne radar data, and in the same month of the year as the 2018 and 2021 airborne radar data. They represent the only known snow density measurements from the Seward Glacier since the 1960s. Snow pit sites were located along surface GPR lines, and near or on airborne radar lines from 2021 and 2023 (Fig. 2). We supplemented our acquired densities with those published by Ochwat and others (2021) for the Kaskawulsh Glacier from 2018.

Three snow pits were dug, with two cores drilled in Snow Pit 1, and one core in each of the other snow pits (Fig. 2). Snow pit density measurements were acquired using a 1,000 cc wedge sampler every ten vertical centimeters in the wall with each sample weighed using an A&D HT1000 digital scale. Snow cores were acquired from the bottom of each snow pit using a Kovacs coring system. The cores were segmented by natural breaks or cut into lengths 10 to 32 cm long, with a mean and median of 20 cm. Each segment of the core was weighed using the same digital scale as for the the pit measurements. An uncertainty of 9% for each density measurement was used, based on work comparing snow density measuring techniques (Proksch and others, 2016). This uncertainty encompasses lost snow when the measuring device was removed, variation in snow density at the top and bottom of the sample, and the presence of ice layers. Column mean densities were calculated by performing a weighted mean using each segment's density and its length as the weighting parameter. The column mean density uncertainty was calculated from the root

mean square of the individual density uncertainties (Ochwat and others, 2021).

2.2.2 Surface GPR data collection and processing

All surface GPR data were collected using a 400 MHz Geophysical Survey Systems Inc. (GSSI) shielded antenna and a SIR 4000 controller. Radar settings for collection were set to continuous mode at 24 scans per second, 2408 samples per scan, and 32 bits per sample. We collected approximately 60 km of common offset data between May 14 and 21, 2023, and hyperbolic analysis surveys on May 17 and 20, 2023.

Common offset data (green lines in Fig. 2) were collected by skiers towing a sled that contained the GSSI radar system. Individual data files were collected for approximately 45 minutes to keep files under 1 GB and to avoid data loss if the controller batteries died. Processing and interpretation were accomplished using the commercially available GSSI software RADAN 7. Data were first processed by applying a time zero correction, followed by clipping out sections of the data when the antennas were stationary. Next, a Finite Impulse Response boxcar filter with a length of 201 scans was applied for background removal. We then applied a horizontal stacking of 20 scans, and lastly a deconvolution. The RADAN 7 deconvolution used four variables, which were: operator length of 31, prediction of five, prewhitening of eight, and overall gain of three. After each file was processed, we combined the individual files from each day into a single file for more consistent interpretations of reflectors. The reflectors were then interpreted using the RADAN 7 layer selection tools. Radar interpretations were performed by manually digitizing ("interpreting") point measurements at the top of the reflector associated with the last summer surface reflector's two-way travel time. This reflector was then compared to the winter snow depth identified in the snow cores.

Hyperbolic analysis surveys are performed over buried objects, such as pipes and poles to measure their depth. As the radar is moved perpendicularly across the pole, changes in the time delay for the radar wave to reflect off the pole create a range hyperbola with the vertex corresponding to the radar directly overhead (Ni and others, 2010). The hyperbolic analysis data were collected near snow pit walls with a metal snow probe inserted 3 m horizontally into the wall. Each survey was 10–12 m in length and crossed perpendicular to the probe at a distance of 2.5 m from the pit wall. Time windows of 100 and 500 ns were used. We used probe depths of 1 and 1.5 m in Snow Pit 1 and 1.2 m in Snow Pit 3. Each hyperbolic analysis file was time zeroed to adjust the top of the scan to the snow surface. The two-way travel time for the interpreted parabola vertex was then exported to be used in radar wave speed calculations.

2.2.3 Real permittivity and liquid water content

Snow density impacts the real permittivity, with higher densities corresponding to a higher real permittivity (Sugiyama and others, 2010). Measurements at 14 sites during a 1965 May and June transect of the Seward, Hubbard, and Kaskawulsh glaciers showed no trend of density to snow layer depth ($R^2 = 0.0003$) and a slight trend of increasing density with increasing elevation ($R^2 = 0.2205$) (Marcus and Ragle, 1970). Based on the work by Marcus and Ragle (1970) and due to the extremely sparse in situ constraints on radar wave speed across the study region we assume a spatially constant density and thus a constant real permittivity.

We calculated the real permittivity from empirical relationships of snow density, and from the hyperbolic analysis two-way travel times. As no empirically derived relationships have been defined for Alaskan snow, we used the mean of nine relationships defined in Table 3 of Sugiyama and others (2010). These empirical relationships were determined under a range of frequencies, snow conditions, and locations. The real permittivity of snow is approximately independent of frequency, especially below 1 GHz, though it is dependent of the water content of the snow (Bradford and others, 2009). An increase of snow density or liquid water content will increase the real permittivity (Bradford and others, 2009; Sugiyama and others, 2010). As such, we used the mean result of the all empirical relationships in Sugiyama and others (2010) to minimize the impacts of local conditions on the density-real permittivity relationship rather than using the relationship with the closest frequency range to our data. The corresponding standard deviation from these nine empirical relationships were used as the uncertainty. Hyperbolic analysis surveys determine real permittivity from the two-way travel time to the parabola vertex and the known depth of the surveyed pole. We calculated the real permittivity using $\epsilon' = ((c * t)/(2 * d))^2$ where c is the speed of light, t is the two-way travel time, and d is the depth of the pole.

Estimates of the liquid water content in the 1, 1.2, and 1.5 m snow columns were achieved by comparing the real permittivity from the hyperbolic analysis results with those derived from the empirical snow density relationships for the same snow column. We used Equation 2 from Sihvola and Tiuri (1986) as this is an empirical relationship that estimates wetness by volume. For the real permittivity values in this equation, we used the mean value derived from the empirical relationships in Sugiyama and others (2010) for the dry snow, and the value from the hyperbolic analysis for the wet snow.

2.3 Surface properties from satellites and weather stations

We used Landsat 8/9 imagery to retrieve end-of-summer snowlines to estimate the ELA for each glacier. Sentinel 1 reflectivity and extrapolated temperature data from weather stations were used to further understand surface properties and melt behavior to enhance our understanding of the radar results.

2.3.1 Equilibrium line altitudes

ELAs were derived using visual identification and manual digitization of the snow to ice transition from Landsat 8 and 9 satellite imagery (Young and others, 2021) from August and September for 2017 through 2023. Snow line interpretations were done at the point where lower elevations were completely (or nearly completely) snow free, similar to the lower snow line bounds in Robinson and others (2025). For each glacier, the mean of all snow lines during this period was used as the ELA due to the frequently overcast study area which causes annual repeat imagery on the same day to be challenging.

2.3.2 Sentinel 1 Reflectivity Analysis

Sentinel 1 is a satellite-based C-band (center frequency 5.4 GHz) synthetic aperture radar instrument which we used to investigate the presence of wet snow (Torres and others, 2012; Nagler and others, 2016). Reflectivity decreases (images appear darker) when wet snow is present (Turbé and others, 2024b). While wet snow can be identified from Sentinel 1 imagery, the bulk liquid water content is not, since when water is present the C-band radar wave only penetrates a few centimeters (Turbé and others, 2024a; Rott and Nagler, 1993). The VV reflected power from accumulation areas has been observed to significantly drop with the onset of melting (Turbé and others, 2024a; Gagliano and others, 2023). We used the Sentinel 1A single-look complex (SLC) product in interferometric wide (IW) swath mode, retrieved from the Alaska Satellite Facility Vertex Data Portal (ASF DAAC, 2024). A descending orbit frame was selected with path number 116 and frame number 391 for the period September 2017 to September 2023 with a nominal repeat time of 12 days. We opted to use a single descending frame as this footprint covers the area of interest at a single capture time (15:48 UTC; 6:48 am local time) removing the need to factor in variable acquisition times when comparing reflectivities. Images were radiometrically terrain corrected based on topography using the built-in processing from the Alaska Satellite Facility. We only included DEM matching for the optional processing. We used the VV polarization gamma power levels and converted to decibels using $\mathrm{dB} = 10 \log_{10}(\mathrm{gamma})$. A value of -26 dB was used for the noise equivalent sigma zero (systematic image

noise), wherein we set all lower values to -26 dB (Torres and others, 2012; Kellndorfer and others, 2022). Then, we used circles of 6 km in diameter to create a time series of the VV reflectivity at different locations for the September 2017 to September 2023 period. We used the VV reflectivity as it has a higher returned power, and unlike VH did not go below the noise equivalent sigma zero value for extended periods (Fig. S2).

2.3.3 Weather station data

In situ measurements of temperature data are sparse in the study region. We used data from the Yakutat airport (59.5033° N, 139.6603° W, 10 m a.s.l.) (National Weather Service, 2024) and Tana Knob automated weather station (69.9081° N, 142.6978° W, 1050 m a.s.l.) (Western Regional Climate Center, 2024) to complement the Sentinel 1 results. While these sites are off-ice and at low elevations, they represent the highest elevation, long-term, accessible, in situ temperature data from the region. Temperatures in the accumulation areas were estimated by applying a lapse rate to the weather station values. We primarily used the Yakutat weather station as Tana Knob had missing data for several days prior to and during the 2018 airborne data acquisition. Temperature lapse rates over glaciers range seasonally between -4 and -10 °C km^{-1}, with typical values between -5 and -7 °C km^{-1} (Cuffey and Paterson, 2010). We use the lapse rate range of -5 and -7 °C km^{-1} to estimate temperatures at elevations of 1200 m a.s.l. and 2000 m a.s.l. 1200 and 2000 m a.s.l. respectively approximate the bottom and top elevations of the main accumulation area of the Seward Glacier, which is the glacier with the most data in our study.

3 RESULTS

3.1 Airborne radar data

Interpretations of the airborne radar data provide measurements of the last summer surface and overlying snow depth across the region of study. The last summer surface was interpreted for 350 line-km in 2018, 1,214 line-km in 2021, and 312 line-km in 2023. The amount of surveyed line-km and glacier coverage varied between the survey years due to time constraints and target objectives. An example of the airborne radar data near the Seward cores is shown in Fig. 3c.

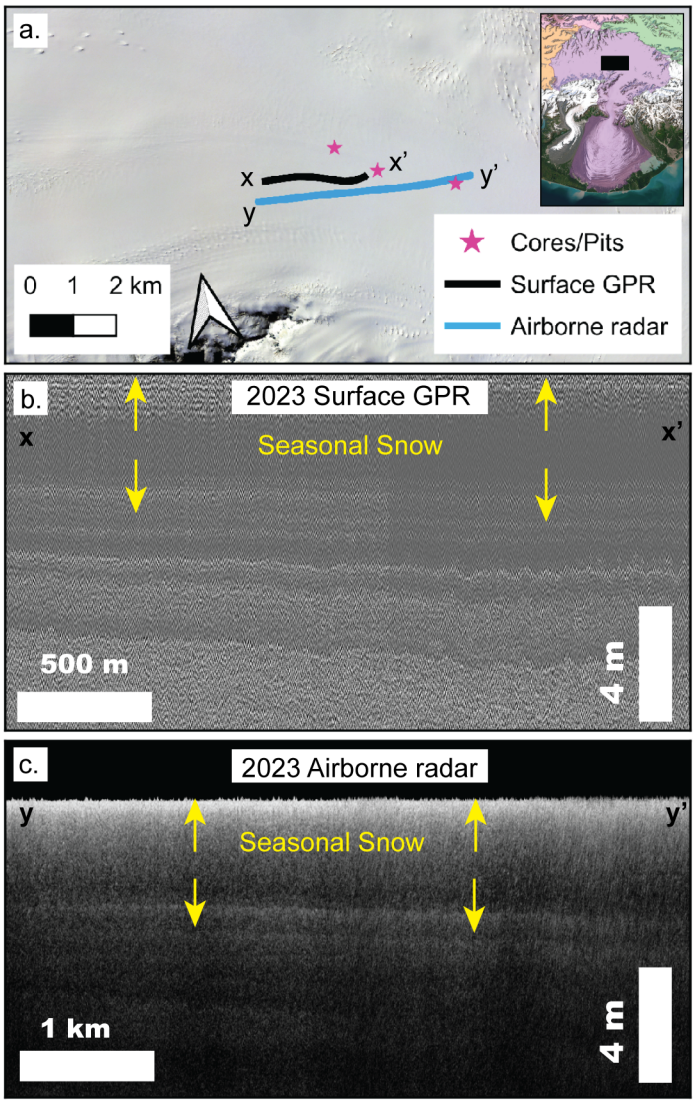

Fig. 3. (a) Sample radar data tracks on the Seward Glacier near the 2023 core sites. The inset shows the Seward Glacier with the extent of panel (a) marked by the black box. Radargrams for (b) surface GPR and (c) airborne radar. Both are read left to right from x/y to x'/y' as marked in (a). The yellow arrows mark the seasonal snow layer. In both radargrams, a layer is present above what we mark as the last summer surface. Based on context from the nearby cores, the reflector marked by the yellow arrows is a better fit for the last summer surface depth than the shallower reflector (Section 3.1.3). The layer above the last summer surface reflector may be related to a surface-wetting event in Fall 2022. Both radargrams are flattened so that the surface is at zero depth.

3.1.1 Crossover analysis of snow depth

Crossover analysis shows that our interpretations are self-consistent. The 2018 data contained eight crossover points with a median difference of 5.8% (21.6 cm) and a mean difference of 6.4% ± 4.8% (22.1 ± 17.1 cm). The 2021 data contained 120 crossover points with a median difference of 3.6% (11.0 cm) and a mean difference of 5.5% ± 6.3% (15.5 ± 16.2 cm). The 2023 data contained 43 crossover points with a median difference of 1.9% (8.2 cm) and a mean difference of 4.1% ± 7.2% (17.6 ± 32.1 cm). For the 2021 and 2023 data, two thirds of the crossover points had a relative difference less than the mean (Figs. S3-S5). The mean from all crossover results (2018, 2021, and 2023) in two-way travel time is 1.49 ns.

Comparison between the 2023 surface and airborne data supports that the two systems detected the same last summer surface. There were 23 crossover points with a median difference of 6.2% (33.1 cm) and a mean difference of 8.1 ± 9.0% (34.3 ± 24 cm) (Fig. S6). This crossover result shows a larger difference between the systems than those from within a year's airborne data. This difference is further explored in the Discussion (Section 4.2). At all but two crossover points, the surface GPR detected a deeper reflector than the airborne radar.

3.1.2 Comparing interpreted depths

Our interpretations are deeper than those of Li and others (2023) for 2018 by a median difference of -2.5% (-9.4 cm) and a mean of -3.0 ± 8.7% (-8.3 ± 30.2 cm); and for 2021 a median difference of -3.7% (-11.4 cm) and a mean of -6.4% ± 30.8% (-17.6 ± 34.3 cm). Spatial distribution is shown for 2018 (Fig. 4a) and 2021 (Fig. 4b). Both the mean and median shows that our study has a slight systematic bias toward deeper interpretations than Li and others (2023). The upper Kaskawulsh and the Seward-Bering divide in 2021 are two locations where interpretations continuously diverged. An example of the divergent interpretations is shown for the upper Kaskawulsh (Figs. 4c, 4d). Further analysis of these difference in interpretations are explored in the Discussion (Section 4.2).

3.1.3 Comparison to cores

Ochwat and others (2021) identified the last summer surface at a depth of 4.2 m in their 2018 Kaskawulsh cores. The nearest ~600 radar samples to the core have a mean two-way travel time of 33.9 ± 0.73 ns. The 1.49 ns mean result from the crossover analysis is added into the uncertainty propagation when converting to snow depth. Using ϵ' = 1.86 ± 0.12 (calculated in the in situ measurement results) a depth of 3.73 ±

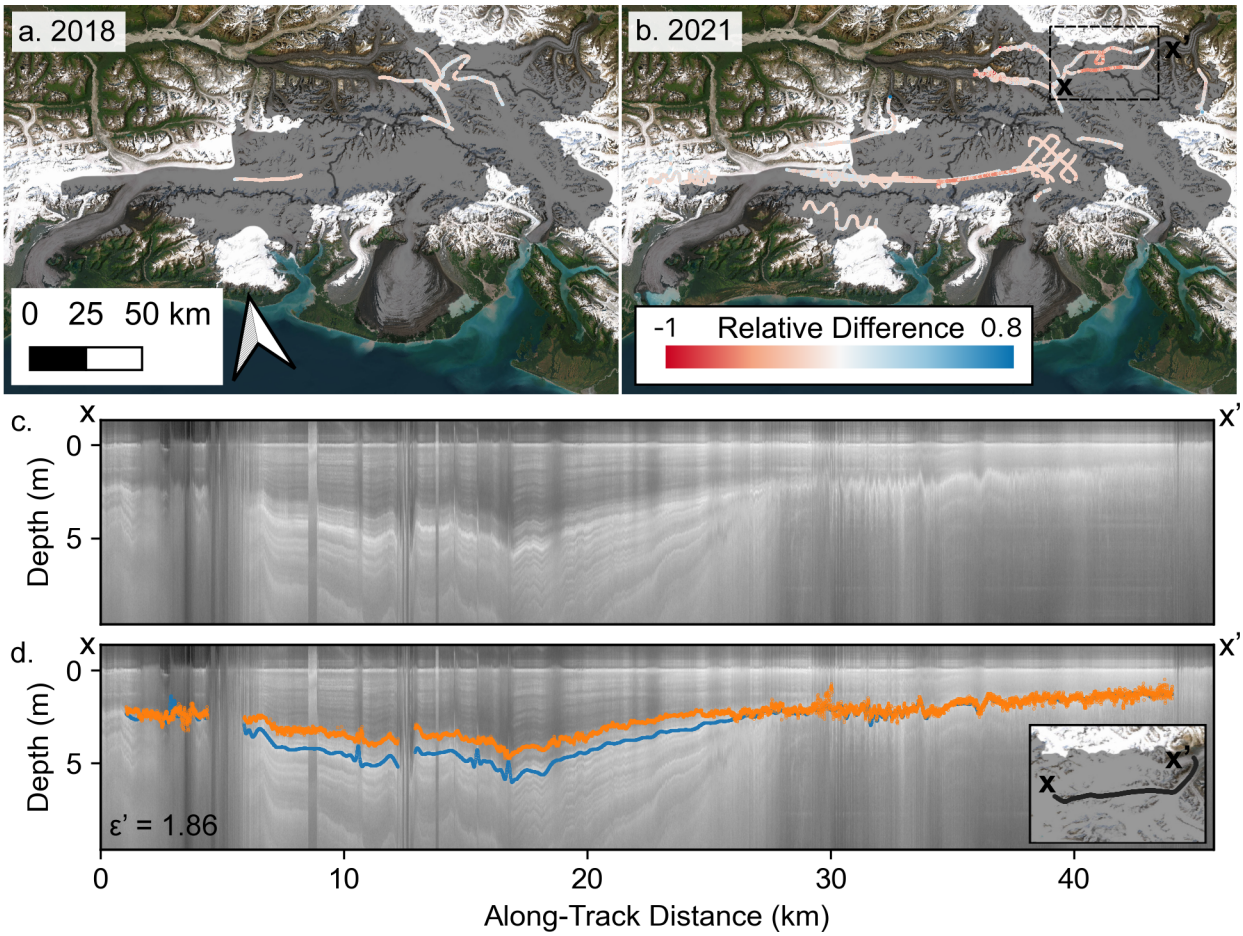

Fig. 4. Comparison between our interpretations and those of Li and others (2023) for (a) 2018 and (b) 2021 show that ours tend to be deeper (negative values) or near zero difference. (c) Radargram from 2021 on the Kaskawulsh Glacier and (d) with annotations. The radargrams are flattened so that the surface is at zero depth. The blue lines are our interpretations, and the orange lines are those from Li and others (2023). Inset in (d) is the radargram path from x to x' with. The gray shading in (a) and (b) is the composite of the glacier outlines in Fig. 1.

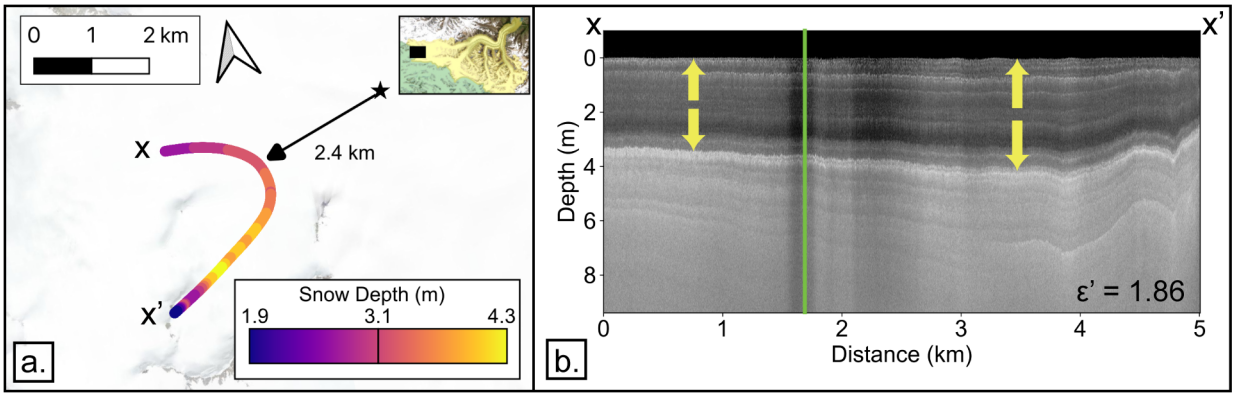

Fig. 5. (a) Snow thickness for the closest 2018 airborne radar data to the Kaskawulsh core (black star). The inset shows the Kaskawulsh Glacier with the extent of panel (a) marked by the black box. (b) Radargram segment with the seasonal snow layer marked by the yellow arrows, and the closest approach to the core marked by the green line. The radargram is read from x to x' in (a) and is flattened so that the surface is at zero depth.

Table 1. Along-track SWE minimum, 1st and 3rd quartiles, and maximum value for each year in units m w.e.

Year	Minimum	1st Quartile	3rd Quartile	Maximum
2018	0	1.3	1.9	3.0
2021	0.2	1.3	2.0	3.4
2023	1.1	1.6	2.0	3.3

0.27 m was obtained for the closest radar approach (Fig. 5a).

We identified the last summer surface at a depth of 4.4 m from our 2023 in situ work (Section 3.2.1.). The mean two-way travel time for the airborne data within one kilometer of any of the 2023 cores was 42.45 $\pm$ 2.12 ns. The 1.49 ns mean result from the crossover analysis is added into the uncertainty propagation when converting to snow depth. Using $\epsilon' = 1.86 \pm 0.12$, a depth of 4.67 $\pm$ 0.42 m was obtained. The snow pit depth falls within the airborne radar snow depth uncertainty. This result supports our selection of the chosen reflector to be the last summer surface, and indicates that the shallower reflector visible in both surface and airborne radar data (Fig. 3) is more recent than the last summer surface.

3.1.4 Glacier average SWE and mass estimates

Spatial visualizations of our along-track SWE values are shown in Fig. 6 for each survey year. We typically observed higher along-track SWE values closer to the coast. We summarize the along-track SWE value ranges, and the first and third quartiles in Table 1.

The SWE values and uncertainty for each 50 m elevation bin are shown in Fig. 7. Uncertainty propagation is discussed in detail in the Supplementary material section 4.2. Bering, Seward, and Hubbard

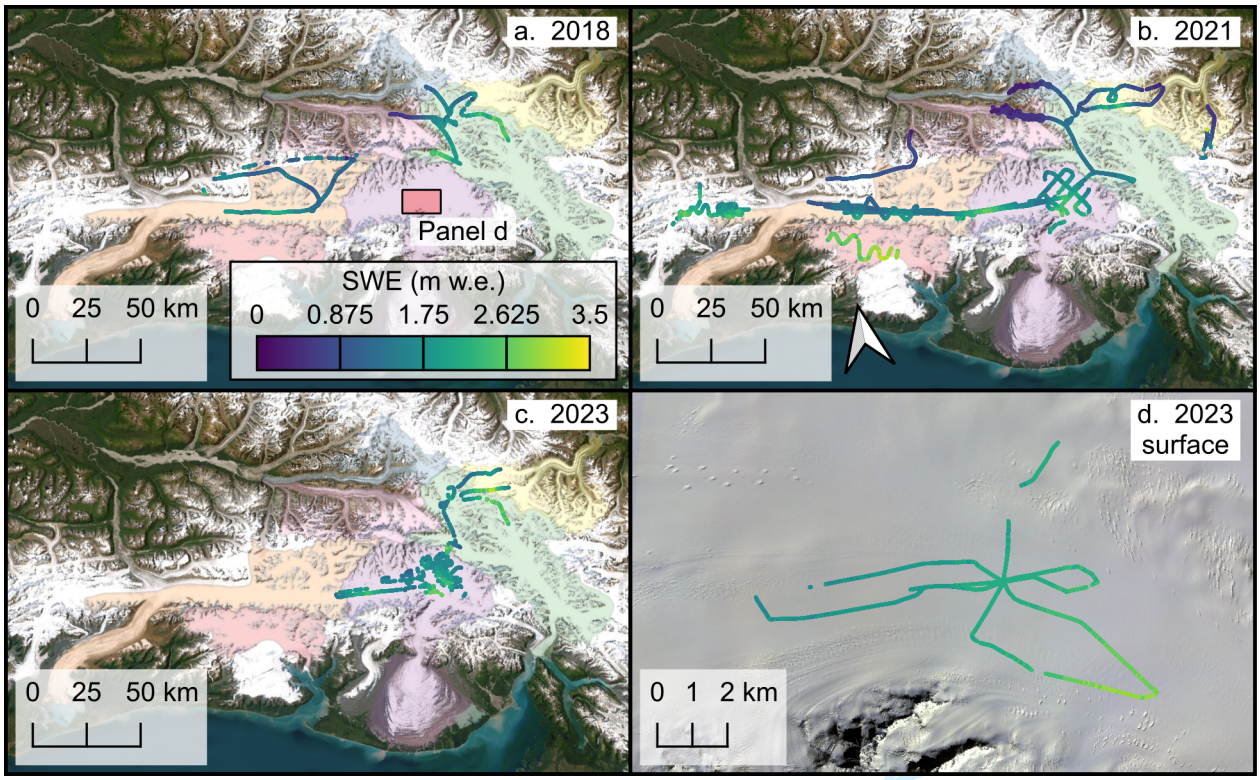

Fig. 6. Along-track SWE from airborne radar for (a) 2018, (b) 2021, and (c) 2023 and the (d) surface GPR. All panels use the same color scale. Panels (a)-(c) use the same extent as in Fig. 1. Background in (d) is PlanetLab satellite imagery from May 16, 2023.

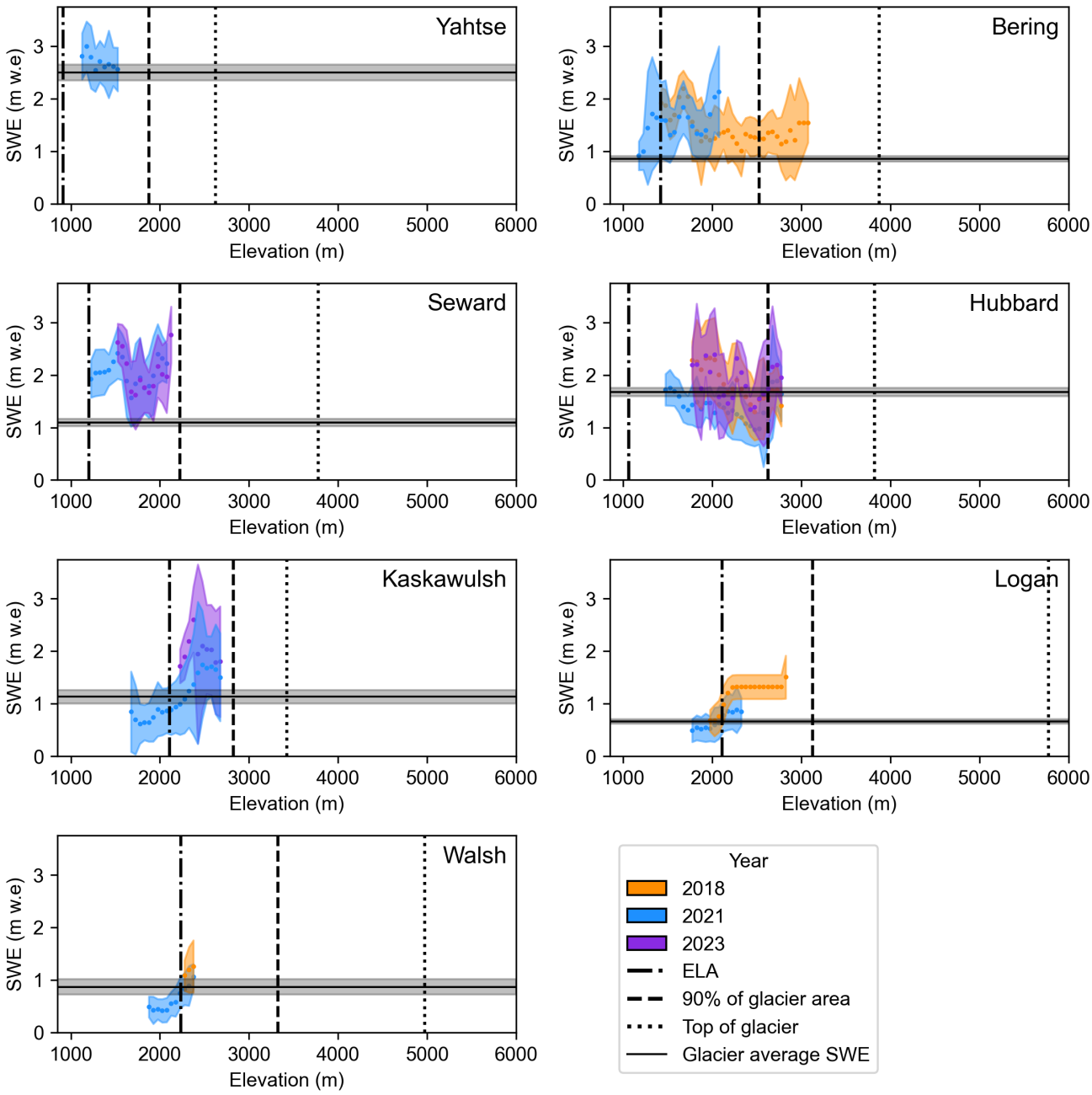

Fig. 7. SWE values for each elevation bin. Shading represents the uncertainty, derived from the standard deviation of all SWE values at that bin, the value of the crossover analysis, and the uncertainty on the the snow density. Here we used 2σ for the uncertainty shading. The glacier average SWE value distributes the input mass to the accumulation area over the total glacier area, which causes the this value to be lower than most elevation bin values. Vertical lines mark the ELA, where the total amount of glacier elevation at or below that elevation bin is 90% and 100%. Fig. S7 shows the equivalent figure including the interpolation to the Mt. Logan cores for the sensitivity test while Fig. S8 shows only the radar data with no interpolation between elevation bins.

show intervals of significant SWE decreases with increasing surface elevation, likely due to orographic shadowing. These glaciers have significant mountains to their southern, more coastal side, with peaks up to ∼3 km higher than the major accumulation areas (Fig. S1). Logan, Walsh, and Kaskawulsh in 2021 show a consistent trend of increasing SWE with elevation, which was not seen on the other glaciers. We hypothesize that Logan, Walsh, and Kaskawulsh are less likely to be impacted by orographic shadowing due to their increased distance from the coast. We further discuss orographic shadowing in the Discussion (Section 4.4).

We report the winter mass balance glacier average SWE for each glacier in Fig. 8 and Table S2. The highest glacier average SWE was found at Yahtse in 2021 at 2.4 ± 0.1 m w.e. The lowest glacier average SWE occurred for Walsh (0.59 ± 0.12 m w.e) and Logon (0.52 ± 0.08 m w.e) in 2021. We also observed that the SWE per elevation bin (Fig. 7) was lower for Walsh and Logan than the other glaciers for the same elevation. Walsh and Logan are the two most inland glaciers in the study area, which due to the distance from the Gulf of Alaska and blocking mountains, containing some of the steepest coastal mountains in the world, results in less available moisture. Due to the relatively small range of surface elevation sampled by the airborne radar, especially for Walsh, these two glaciers may also be less well constrained by our measurements.

The winter mass balance in units of mass of water (Figs. 9, S9, and Table S2) revealed a similar trend as the glacier average SWE values. Yahtse, Bering, Seward, and Hubbard have significantly higher input mass than Kaskawulsh, Logan, and Walsh.

The sensitivity test including the Mt. Logan core data did not have a significant impact on the majority of the results. While several of the glaciers reach much higher elevations than the range sampled by the radar, those high elevations zones represent a small portion of the total glacier area (Figs. 7, S10, Table S4). Walsh is the only glacier where the sensitivity test had results that were outside the 2σ uncertainty of the radar only estimation. This was probably due to the 2018 Walsh data where only 150 meters of vertical extent were sampled by the airborne radar (Fig. 7). The limited vertical extent that was sampled likely caused the 2018 Walsh estimates to be more sensitive to the Mt. Logan core data than the other glaciers. In 2021, for Walsh, the sensitivity test was within the 2σ uncertainty of the radar only estimation. For the mass of water, the sensitivity test result for Walsh (Fig. 9) was slightly outside the radar only 2σ uncertainty. For the other six glaciers, the sensitivity test result fell within the radar only estimation 2σ uncertainty. If a large enough elevation range and surface area is sampled by airborne surveys, capturing

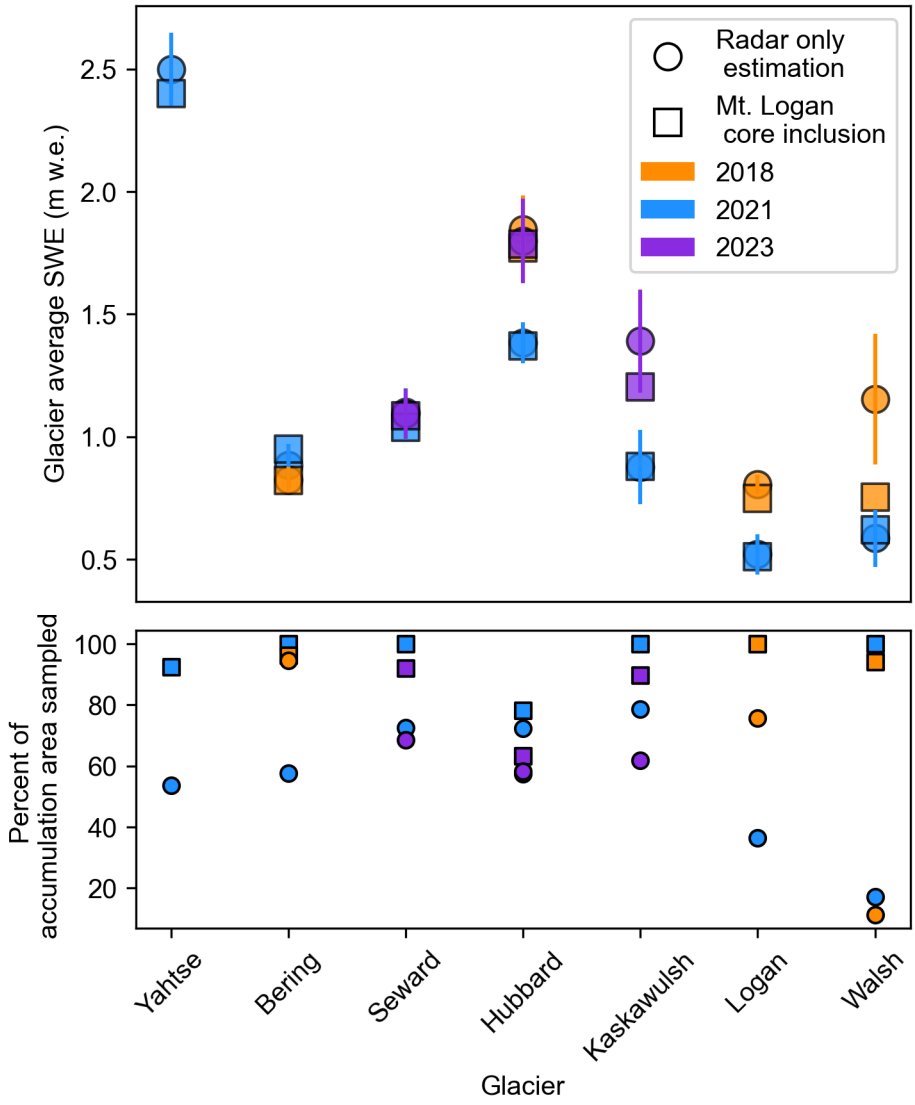

Fig. 8. (a) Glacier average SWE for each glacier and survey year (b) and corresponding percent of accumulation area sampled. Glaciers are ordered roughly by their distance from coast, closest (left) to further (right). In this plot we show the 2σ uncertainty for the radar only estimation. The percent of the accumulation area sampled is the sum of the areas for each hypsometry elevation range that contains radar-derived SWE values divided by the glacier area above our defined ELAs. For the Mt. Logan core inclusion estimation, the percent of accumulation area sampled includes the glacier area above the highest surface elevation with radar data.

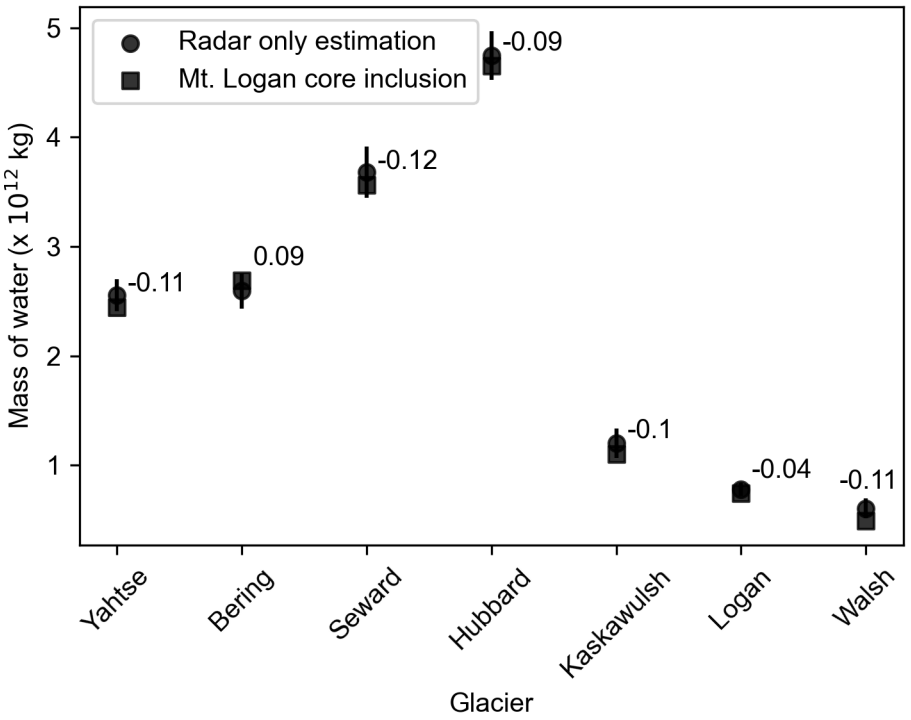

Fig. 9. Input mass of water for each glacier's accumulation area. Glaciers are ordered roughly by their distance from the coast, closer (left) to further (right). The values on the plot for each glacier are the difference between the radar only estimation and the estimation when including the Mt. Logan core data. The estimations that include the interpolation to the Mt. Logan core record lie within the uncertainty of the radar only estimation. Values are reported in Table S3 and the yearly mass estimates are shown in Fig. S9. In this plot we show the 2σ uncertainty for the radar only estimation.

the highest glacier elevation snow depth/SWE is not critical for constraining the winter mass balance.

3.2 In situ and surface-coupled measurements

3.2.1 Snow densities

Pits were dug to 1.6–2.4 m deep with cores drilled in the bottom of snow pits for a total depth of 5.84–7.41 m (Fig. S11, Table S1). All cores were depth limited by an ice layer that neither the drill or a snow probe could penetrate. The ice layer that stopped the drilling was likely the 2021 summer surface. No annual dust layers were visible in the cores. However, an ice layer at approximately 4.4 m deep in pit two was found to be very hard, but penetrable. We used this ice layer depth as the estimation of the last summer surface depth. Thin ice lenses of varying thickness and horizontal spread were also observed at several locations in the snow pits, and were especially concentrated around a depth of approximately 50 cm (Figs. S12, S13).

Table 2. Real permittivity (ϵ') from the 2023 hyperbolic analysis surveys and snow densities, along with the estimated snow wetness by volume. We calculated the real permittivity from snow densities for the snow pit each hyperbolic analysis was collected in (survey pit), and when using the mean snow density from all three snow pits (all pit). The all pit real permittivity was used for estimating the volumetric wetness. Uncertainties on the real permittivity are from the standard deviation of the nine empirical relationships from Sugiyama and others (2010) and the standard deviation of the density.

Probe depth (m)	Hyperbolic analysis survey ϵ'	Survey pit density (kg m^{-3})	Survey pit ϵ'	All pit density (kg m^{-3})	All pit ϵ'	Estimated wetness by volume %
1	3.52 ± 0.09	353 ± 32	1.69 ± 0.13	364 ± 33	1.71 ± 0.13	11.7 ± 0.7
1.2	2.74 ± 0.07	375 ± 34	1.73 ± 0.13	371 ± 34	1.72 ± 0.13	7.8 ± 0.8
1.5	2.75 ± 0.02	369 ± 33	1.72 ± 0.13	382 ± 35	1.75 ± 0.14	7.7 ± 0.8

Using the seasonal snow layer depth of 4.4 m, the mean seasonal snow density from all Seward data was estimated to be 425 ± 38 kg m^{-3}. As a sensitivity test we also calculated the mean snow density to depths of 3.9 m (420 ± 39 kg m^{-3}) and 4.7 m (430 ± 38 kg m^{-3}). The small variability in mean snow depth for these different column depths shows that error in measuring or estimating the physical snow depth does not significantly change the estimated seasonal snow density. Our snow layer depth of 4.4 m (1.9 m w.e.) compares well to measurements from Marcus and Ragle (1970) collected on the Seward Glacier from May 21 to 22, 1965 of 4.6 m (1.7 m w.e.) at 1370 m a.s.l. and 5.8 m (2.1 m w.e.) at 1765 m a.s.l. The SWE from our cores are also consistent with a physical model-based approach to estimating surface mass balance from spatiotemporally sparse observations of surface speed and ice geometry also provides a similar estimate for annual average mass accumulation rates (Brinkerhoff and others, 2025).

3.2.2 Surface GPR

Table 2 summarizes the results from the hyperbolic analysis surveys and the corresponding estimations from the empirical relationships using the mean density to that depth. The density and thus real permittivity varied only slightly between the survey pit and the three-pit mean. The real permittivity used for converting the airborne radar/surface GPR two-way travel time to snow depth was calculated from the mean density from all snow pits. The permittivity from the 1 m probe depth hyperbolic analysis result was higher than that for the 1.2 and 1.5 m probe. This was unexpected from a dry snow estimation as the 1 m depth had a lower column density. Additionally, the 1 m probe had a significantly higher real permittivity than that derived from the density. The increased real permittivity for the 1 m probe was likely due to near surface

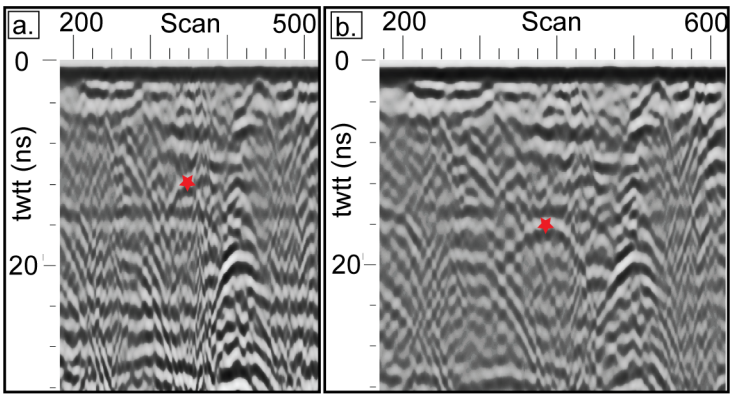

Fig. 10. Hyperbolic analysis surveys for the probe at depths of (a) 1 m and (b) 1.5 m. The vertex of each hyperbola caused by the probe is marked by a red star. The column of parabolas at roughly scan 400 in (a) and 500 in (b) did not change as the probe depth was changed. Thus we attribute these parabolas to the snow pit wall.

meltwater, which is further explored in the Discussion (Section 4.3). We show examples of the hyperbolic analysis data in Fig. 10. As expected, no significant difference in radar speed arose from the different time windows. The two-way travel time and the corresponding real permittivity for each survey are reported in Tables S5-S7.

We identified the last summer surface for approximately 47 of the 60 line-km of collected common offset surface GPR. The last summer surface tended to not be retrievable from snow-bridged crevasses and when descending steeper slopes (only impacted a few line-kilometers of surface GPR to the northeast of the 2023 cores). While reflectors were observed over snow bridges they were not clear or consistent enough to be interpreted. We show an example of the surface GPR and in Fig. 3b. The along track SWE estimates derived from the common offset data are shown in Fig. 6d. The surface GPR returned a depth of approximately 4.52 $\pm$ 0.19 m at the closest approach to Snow Pit 2 (uncertainty calculations shown in the Supplementary material section 4.1), where the last summer surface depth of 4.4 m was identified via snow probe. This implies that the surface GPR interpretations are correct and that a dry snow approximation is fair as the depth of 4.4 m falls within the surface GPR uncertainty. The snow column stratigraphy for the surface GPR was similar to that of the airborne radar (Fig. 3).

3.2.3 Real permittivity and liquid water content

The seasonal snow density for Seward was 425 $\pm$ 38 kg m^{-3} from our work providing ϵ' = 1.83 $\pm$ 0.14, and for Kaskawulsh was 450 $\pm$ 21 kg m^{-3} from Ochwat and others (2021) corresponding to ϵ' = 1.89 $\pm$ 0.13. We used the mean of these two surveys, which was 438 $\pm$ 22 kg m^{-3} resulting in ϵ' = 1.86 $\pm$ 0.12, as our characteristic density and real permittivity. These values were used to convert the radar two-way

travel times to snow depth and SWE. Our mean value was within the accepted values for dry snow of 1.5–2 (Wu and Liu, 2012). The similar densities for the snow column on the Kaskawulsh (more inland) to that on Seward (more maritime) support the use of a single value. Our real permittivity also compares well to the values determined by McGrath and others (2015) of 1.78–2.06, with a mean of 1.89, derived from measurements on six Alaskan glaciers outside of the St. Elias Mountains.

We report the liquid water content estimates from each of the hyperbolic analysis surveys in Table 2. They show a decrease in liquid water content by volume with increasing depth, with the largest decrease occurring between 1 and 1.2 m, implying that the liquid water was mostly restricted to the upper section of the snow column. The liquid water content is further explored in the Discussion (Section 4.3).

3.3 Surface properties from satellites and weather stations

3.3.1 Equilibrium line altitudes

ELA elevations were observed to be lower for glaciers closer to the coast (Fig. S10 and Table S8). The two tidewater glaciers in our study, Yahtse (ELA: 912 ± 91 m a.s.l.) and Hubbard (ELA: 1061 ± 24 m a.s.l.) have the lowest ELAs. The most inland glaciers (Kaskawulsh, Logan, and Walsh) have the highest ELAs around 2100–2200 m a.s.l. Many late-summer snowlines such as on Yahtse, Hubbard, Seward, and Kaskawulsh occurred in or near crevasse fields/ice falls, challenging the retrieval of the late summer snow lines and increasing uncertainty in the interpretations.

For Kaskawulsh and Hubbard, existing ELA estimates allow for comparison which show that our ELA estimates are robust and suitable for restricting the radar data to the accumulation area. For Kaskawulsh, we calculated a mean of 2106 ± 100 m a.s.l., similar to a mean of 2261 ± 151 m a.s.l. for 2013-2019 estimated by Young and others (2021). For Hubbard, we calculated a mean of 1061 ± 24 m a.s.l., similar to ∼1000 m a.s.l. from the late 1960s from Trabant and others (2003).

Further support for our ELA estimations arose from the airborne radar data where dipping reflectors were observed near the ELAs. We show one such example from the Logan Glacier in 2018 in Fig. 11. These dipping reflectors showed a decreasing layer thickness as they approached the ELA. Below the winter's snow accumulation, the previous year's firn layer was observed. The interpretable firn layer ends before the ELA, likely due to near ELA snow properties and radar interpretation limits. The selected ELA lines were where the majority of the glacier width was covered by snow, though in places it was patchy snow, which could result in less clear radar stratigraphy when observed as firn the following year.

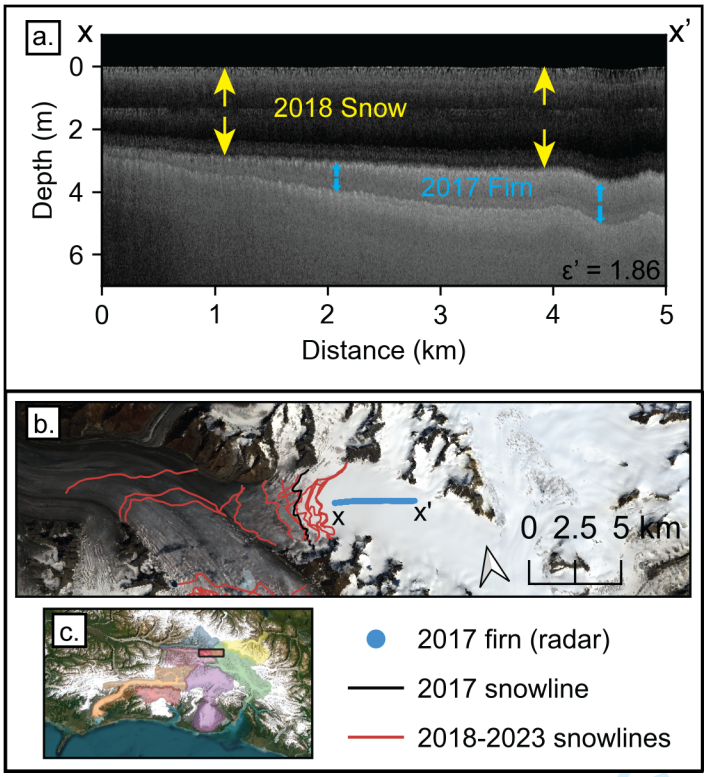

Fig. 11. (a) 2018 airborne radar data on the Logan Glacier prominently shows the 2017 firn layer thinning and disappearing near the (b) 2017 end-of-summer snow line. The radargram is read from x to x' in (b). Radargram is flattened so that the surface is at zero depth. Background is a Landsat 8 image acquired on August 6, 2017. (c) Context map for panel b using the same color shading as in Fig. 1. Subset of (b) is the black box.

Additionally, as the firn layers approach the ELA, they thin. Very thin layers are not easily interpretable as they reach the resolvability limit of radar. We observed thinning firn layers near the ELA for Logan in 2018 and 2021, Kaskawulsh in 2021, and Bering in 2021, but not for Walsh in 2021. No other glaciers exhibited last summer surface reflectors crossing their ELA.

3.3.2 Sentinel 1 Reflectivity Analysis

We show the Sentinel 1 spatial reflectivity for the chosen path and frame image (Fig. 12) and the time series for two locations on the Seward Glacier (Fig. 13). The reflectivity power was higher during the May 2021 airborne data acquisition compared to the other years of data, implying that the snow was drier and the melt had not yet reached the major accumulation areas. This was likely due to the earlier survey dates in 2021.

A significant decrease in returned power was observed from the start of the in situ work on May 14, 2023 (imagery May 11, 2023) to the end of the airborne data acquisition on May 24, 2023 (imagery May 23, 2023) at the 2023 core sites (Fig. 13). This drop, though with a smaller magnitude, was also observed at the Bering-Seward ice divide. Thus by the time of airborne data acquisition in 2023, the whole Seward Glacier area that was sampled by the airborne radar had experienced some melting. Furthermore, at the Seward core site, the time series reveals an increase in reflectivity power in late September 2022, which is then followed by a $\sim$4 dB drop in reflectivity power between October 7, 2022 to October 31, 2022 (Fig. 13). No Sentinel 1 image for the specific frame and path was available from the Alaska Satellite Facility for mid-October 2022.

Based on the increase and then decrease of the reflectivity at the Seward core sites (Fig 13), and weather station data during late September/early October 2022 (Section 3.3.3), we infer that there was a major snowfall event that was then followed by temperatures warm enough to cause melting. As seen by the Sentinel images (Fig.12), the darkening (decrease in reflected power) during October of 2022 was especially prevalent in the lower elevations of the Seward accumulation area. This results in a reflector at shallower depths than the last summer surface reflector (Fig. 3) in the area near the Seward core sites. The reflector we attribute to this melt event was not observed at high elevations, nor did it taper to the reflector we attributed to the last summer surface.

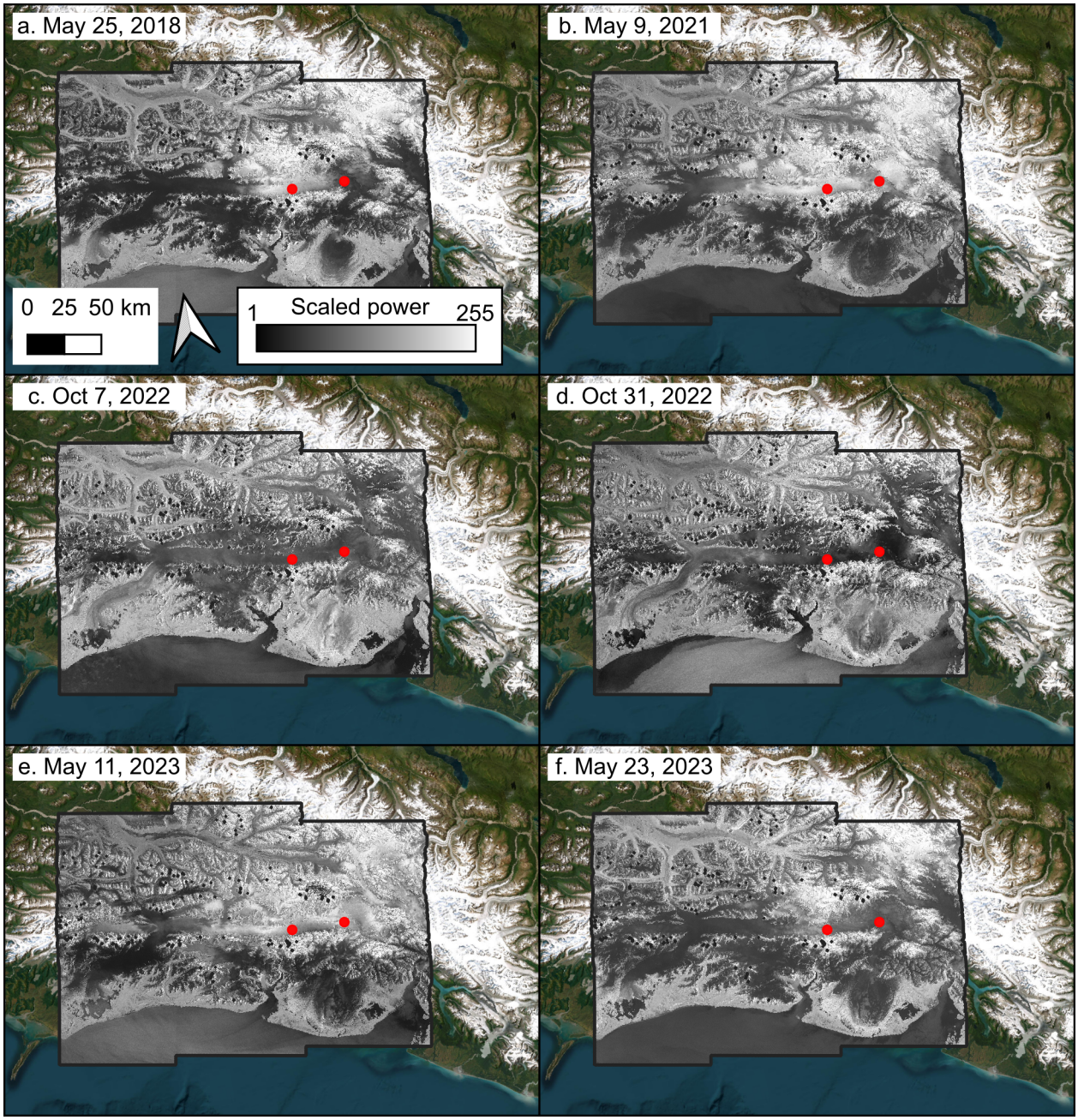

Fig. 12. Sentinel 1 gray scale browse images from the Alaska Satellite Facility approximately during airborne radar acquisition in (a) 2018 and (b) 2021, (c, d) during early Fall 2022, (e) during 2023 surface GPR acquisition, and (f) during the 2023 airborne radar acquisition. The spatial scale and color bar is the same between all panels so we only include them in panel (a). Darker colors represent lower reflectivity. The two points marked on all panels are the sampling locations in Fig. 13 at the 2023 Seward core site and the Seward-Bering ice divide. The black outline is included to mark the edge of the Sentinel 1 image. ASF DAAC 2015, contains modified Copernicus Sentinel data 2015, processed by ESA.

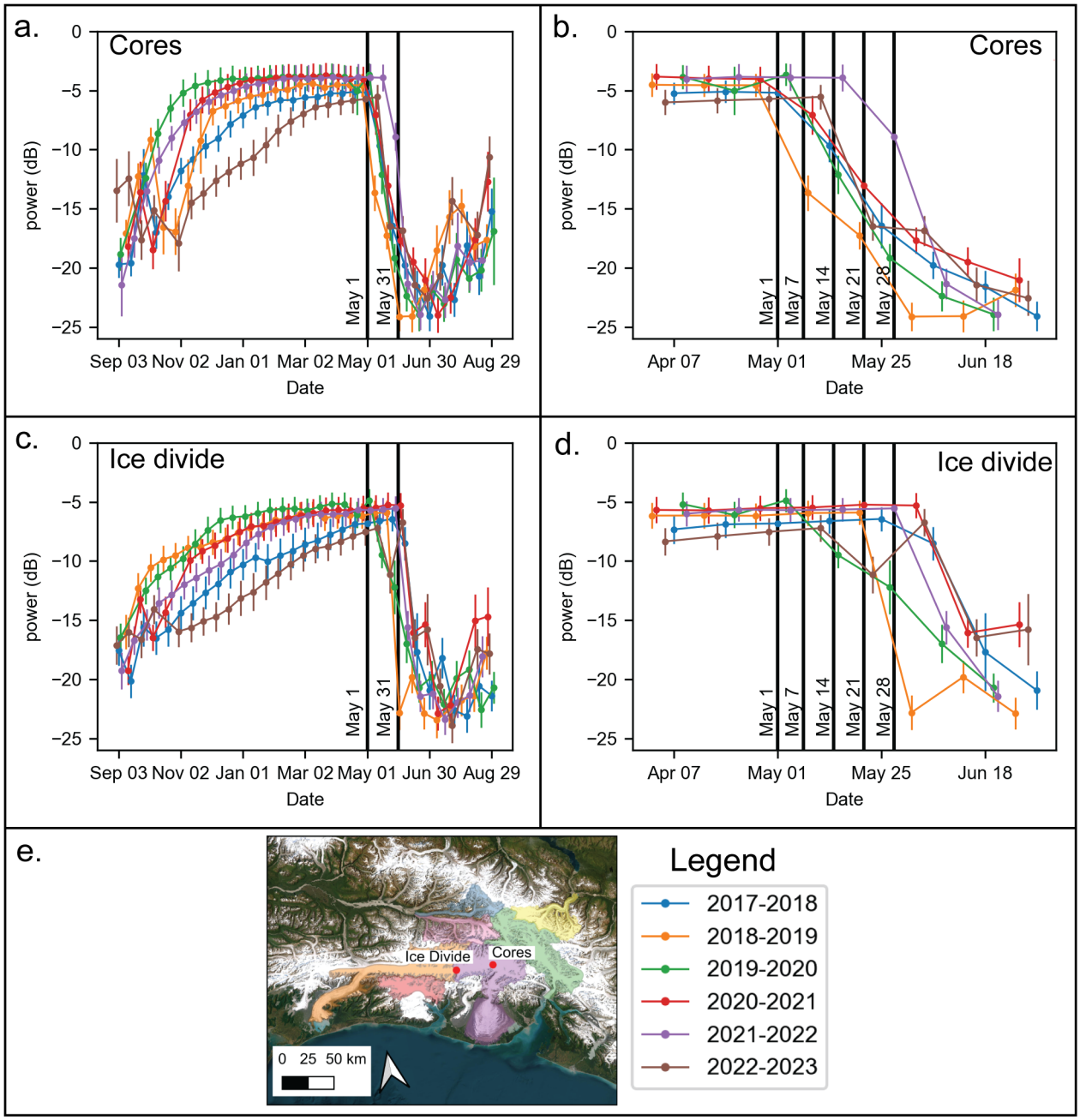

Fig. 13. Reflectivity over six water years for the (a) 2023 Seward core sites at ~1600 m a.s.l. and (b) subset from April 1 to June 30. Same period for the (c) Seward–Bering ice divide at ~2000 m a.s.l. and (d) subset from April 1 to June 30. Error bars are single standard deviation of the power in the sampling area. Vertical lines are labeled with context dates for improved understanding of the time series around May. (e) Context map of the location of the two Sentinel 1 sample sites and the water year color legend.

Table 3. Mean temperatures prior to and during airborne data collection derived from hourly data at Yakutat, Alaska. We also include the estimated temperature at 1200 and 2000 m a.s.l. for the week prior to data collection using a lapse rate of -5 to -7 °C km^{-1} as a range from the minimum to maximum temperature based on the lapse rate range.

Temperature (°C) for:	2018	2021	2023
Two weeks prior mean	8.6 ± 3	5.6 ± 4.9	9.6 ± 3.8
Two weeks prior hourly max	20.6	17.8	23.9
One week prior mean	8.2 ± 2.8	5.2 ± 3.7	10.0 ± 4.4
One week prior mean (1200 m a.s.l.)	-2 – 2.2	-3.2 – -0.8	1.6 – 4
One week prior mean (2000 m a.s.l.)	-5.8 – -1.8	-8.8 – - 4.8	-4 – 0
One week prior hourly max	20.6	13.3	23.9
During data collection mean	8.4 ± 1.8	6.3 ± 2.1	8.2 ± 2.6
During data collection hourly max	12.2	11.7	12.2

3.3.3 Weather station data

We report the mean temperature for the two weeks prior, one week prior, and during the airborne data acquisition for each year. Using typical lapse rates (-5 to -7 °C km^{-1}) for glaciers, the temperatures on Seward were 6–8.4 °C colder at 1200 m a.s.l., and 10–14 °C colder at 2000 m a.s.l. than at Yakutat. Despite the similar airborne survey dates in 2018 and 2023, the temperatures in 2023 were roughly 2 °C warmer in 2023 for the week preceding data collection. From these estimated temperatures for Seward, melt likely occurred across the radar sampled area of the Seward Glacier during the day in 2023 prior to the airborne data collection, while in 2021, due to the earlier surveys, melt was restricted to elevations below the ELA. The temperature time series at Yakutat and Tana Knob reveal similar patterns (Figs. S14, S15), including intense temperature peaks on May 18 in 2018 and 2023. However, the higher mean in 2023 likely caused more significant melting which contributed to the lower quality airborne data retrieval. These temperature results agree with the Sentinel 1 results of more liquid water at the snow surface in 2023. The higher temperature in 2018 than 2021 likely had less of an impact on the 2018 surveys, as that year higher surface elevations were sampled by the airborne radar.

Data derived estimates of melt extent are validated from field observations in May, 2023. Surface melt was observed during the surface data collection, along with sunny and calm daytime conditions. Additionally, while leaving the Seward Glacier on May 23, 2023, several small pools of meltwater were observed to have started forming in the accumulations areas around 1600 m a.s.l. on the Seward and

Hubbard glaciers.

Weather station records provide collaborating evidence to Sentinel 1 data that snowfall occurred, followed by snow compaction and/or melt that caused a secondary ice layer that could be observed by the airborne radar during the 2022-2023 winter. The Tana Knob snow depth measurements showed a significant increase in the daily average snow depth from 103 mm to 594 mm between October 11 to 13, 2022. By October 17, 2022, the average snow depth had reduced to 198 mm. (Fig. S16). Then, snow depths had a fluctuating but increasing trend of depth to 338 mm by October 31. Additionally, temperatures in mid-October were likely high enough to cause melt at the lower elevations in the Seward accumulation basin, consistent with where the Sentinel 1 reflectivity decrease were observed. Using the lapse rate of -5 to -7 °C km^{-1}, the Yakutat weather station had a mean daily temperature of ∼10 °C from October 15-19, 2022 (Fig. S17), which would allow for melting in the region of the 2023 snow cores and surface GPR data collection (1650 m a.s.l., estimated temperatures of 1.75 to -1.55 °C). The Tana Knob temperatures on October 16, 2020 with a mean of ∼3 °C at 1050 m a.s.l. (Fig. S17) also support that melt could have just started to occur at the 2023 snow core sites (1650 m a.s.l., estimated temperatures of 0 to -1.2 °C).

4 DISCUSSION

4.1 Mass input trends

We observed that more maritime glaciers received higher accumulation than the more inland glaciers (Fig. 9, Table S2). The three largest glaciers in our study, Seward (3363 km^2), Bering (3025 km^2), and Hubbard (2834 km^2) (RGI Consortium, 2023) are maritime and have the highest mass input of water in our study area. While high winter accumulation can be counteracted by increased ablation rates, it is logical for the largest glaciers to receive the highest input masses. We also observed that tidewater glaciers (Yahtse, Hubbard) had especially high accumulation compared to non-tidewater glaciers of similar size. The higher input mass of water occurring for the tidewater glaciers is likely in part due to the higher accumulation area to total area ratio compared to non-tidewater glaciers.

Our results determined that Hubbard had the overall highest input mass of all glaciers in our study region, despite not being the largest glacier (third behind Seward and Bering). We do not believe that Hubbard's high input mass is due to a sampling bias that may have resulted from a lack of measurements near the ELA. In 2021, SWE was retrieved to a lower elevation (1500 m a.s.l.) than in 2018 and 2023 (1800 m a.s.l.) and showed increasing SWE in lower elevation bins (Fig. 7), rather than decreasing. Therefore,

assuming spatial trends are consistent across years, extrapolating SWE from our sampled elevations to the zone near the ELA should not lead to an overestimate of the input mass.

Furthermore, as Hubbard is a tidewater glacier while Bering and Seward are land/lake terminating, the main method of mass loss is different. Due to the high frontal ablation rates, tidewater glaciers require high input mass to maintain the same area as a land-terminating glacier. Trabant and others (1991) estimated that 95% of Hubbard's mass loss is due to frontal ablation. We estimated Hubbard's accumulation area to total area ratio to be 0.96, which is much greater than that of the Seward (0.53) and Bering (0.55). Hubbard's high accumulation area to total area ratio supports that it will lose significant mass from frontal ablation rather than surface melting, and will need a higher input mass the Bering and Seward to maintain its large extent.

Yahtse, like Hubbard, is a tidewater glacier that has a higher input mass compared to non-tidewater glaciers of similar size in our study. Though Yahtse had the highest glacier average SWE, due to its smaller size the input mass of water is lower than Bering, Seward, and Hubbard. Also, Yahtse's glacier average SWE of ∼2.4 m w.e. was lower than that of other maritime Alaskan glaciers such as Wolverine and Scott which have mean SWE of ∼2.5–4 m w.e. depending on the estimation method (McGrath and others, 2015). Our value for Yahtse was calculated using solely the snowfall to the accumulation area while those from McGrath and others (2015) included the snowfall to the ablation areas. However, Yahtse's accumulation area ratio of 0.93 means that an estimate of the glacier average SWE that includes the ablation area snowfall will result in only a slightly higher glacier average SWE value, though it would still be on the low end of values reported in McGrath and others (2015).

We hypothesize that the glacier size may impact the end-of-winter glacier average SWE as Scott (141.1 km^2) and Wolverine (16.7 km^2) are respectively one and two orders of magnitude smaller than Yahtse (1019.1 km^2) (RGI Consortium, 2023). Topographic features such as aspect and slope are likely more influential and pronounced on smaller glaciers as small changes in these parameters can greatly impact snow deposition, especially though avalanches and wind drifting. While our airborne radar surveys did not sample the edges of glaciers, due to the significant widths (up to ∼5 km), the processes occurring at the edges should have minimal impact on the overall glacier input mass and accumulation trends.

4.2 Uncertainties in airborne interpretations

Here we discuss differences between the airborne radar, the 2018 Kaskawulsh core, interpretations from Li and others (2023), and the 2023 surface GPR.

The closest 2018 airborne radar data depth (3.73 $\pm$ 0.27 m) to the Kaskawulsh core was slightly shallower than the measured snow depth in the core (4.2 m) (Section 3.1.3). We assumed that the airborne radar detected the same last summer surface as identified in the core and that the difference in depth is a physical difference. Core stratigraphy from Ochwat and others (2021) does not show prominent ice layers above the last summer surface, so it is unlikely that a shallower ice layer was detected by the airborne radar. If we were to constrain the airborne radar snow depth at closest approach to the core to be 4.2 m, it would imply a real permittivity of 1.47 $\pm$ 0.19, which corresponds to a snow density of approximately 250 kg m^{-3}, which is significantly less than the 450 kg m^{-3} observed from the core. We believe that it is more probable that there are variations in snow depth at scales of several kilometers than the snow density varying by a factor of nearly two. Because most of the 2018 airborne data could be continuously detected and interpreted from the closest approach to the Kaskawulsh core, we therefore assumed that the reflector elsewhere was also the last summer surface. Discontinuous reflectors, such as on the Bering Glacier, had similar appearances to that of the one near the core, so we also assume those reflectors are the last summer surface.

Comparing our interpretations to those of Li and others (2023), we identified two areas with significant differences in the 2021 data: upper Kaskawulsh and the Seward-Bering ice divide (Fig. 4) (Section 3.1.2). At the Seward-Bering ice divide, multiple radar tracks were acquired in 2021, and only one radar track was significantly different in interpretation between the two studies. We favor this study's interpretations at the Bering-Seward ice divide due to our interpretations having better depth consistency between the multiple radar tracks.

For the upper Kaskawulsh in 2021, due to the lack of constraints from other radar data tracks and in situ data, it was not clear which reflector corresponded to the last summer surface. It is known that rain on snow events can cause uncertainties in detecting the last summer surface (McGrath and others, 2015), but this disagreement zone occurs at high elevations where we expect rain on snow events to be less likely to occur. Another possibility was that a late summer/early fall snow event occurred on the upper Kaskawulsh which was then followed by warmer temperature causing multiple ice layers to form, complicating the stratigraphy similar to Fall 2022 at the lower elevations on the Seward Glacier. However,

we did not observe a decrease in Sentinel 1 reflectivity in the fall of 2020 at the Kaskawulsh core site that would have indicated liquid water that later formed an ice layer (Fig. S18). Currently, we do not have a compelling argument for whether our study's interpretations, or those from Li and others (2023) are the correct ones for this section of the Kaskawulsh Glacier in 2021. Our interpretations are of a brighter reflector (Fig. 4) than the interpretations from Li and others (2023), however brightness of a reflector is not conclusive evidence for indicating the last summer surface. The upper Kaskawulsh in 2021 is a good example of the subjectivity that is necessarily involved when interpreting such radar without in situ constraints.

Li and others (2023) also showed that the airborne radar system can retrieve multi-year to multi-decadal layering of snow. While we observed some reflectors deeper than our interpreted last summer surface at the higher elevations in our study, such as the Seward-Bering ice divide and the upper Kaskawulsh Glacier, we do not include these reflectors in our analysis as they were not interpretable throughout the accumulation areas. Our in situ data gives us confidence that our interpretations represent the last summer surface and not the deeper reflectors which would represent multiple years of accumulation.

Comparison of the 2023 airborne radar to the surface GPR showed that the airborne radar has the capability of detecting the last summer surface at similar depths to the surface GPR. Crossover analysis between the airborne radar and surface GPR showed a mean difference of 34.3 $\pm$ 24 cm (Section 3.1.1). This is similar to the mean crossover difference in depth for each year of airborne data (Section 3.1.1) with 2018 at 22.1 $\pm$ 17.1 cm, 2021 at 15.5 $\pm$ 16.2 cm, and 2023 at 17.6 $\pm$ 32.1 cm. Therefore, within the accuracy of our interpretations, the airborne radar and surface GPR were the same feature. The difference in interpreted depths may be in part due to to melt and compaction which lowered the surface $\sim$25 cm, as observed with bamboo stakes during the 2023 surface work (May 14–22). However, for two crossover locations the airborne radar returned a larger depth. When excluding these two points, there was a weak correlation of $R^2 = 0.09$ between the number of days between the surface and airborne data and the difference in measured depths. If the surface melt and compaction were the key contributor to the different depths, we would have seen a strong correlation between the difference in interpreted depths and the time between observations. Compaction from the surface GPR system during measurements is unlikely to cause significant changes to the measured snow column, as there was minimal change (on the order of a few centimeters) in snow depth from the ski and sled track compared to the undisturbed adjacent snow. While light rain and snow occurred on May 19th, 2023, it resulted in minimal accumulation and could

not counteract the surface compaction/lowering. The difference in depths is also unlikely to be due to the vertical radar resolutions. The 400 MHz radar had a resolution of ∼14 cm (1/4 wavelength, with an in-snow wavelength of ∼55 cm (Knight and others, 2004)) using ϵ' = 1.86 (v = 0.22 m ns^{-1}). Both the surface GPR, and the airborne radar with the vertical resolution of ∼3 cm (Li and others, 2019; Rodriguez-Morales and others, 2021), have vertical resolutions less than the crossover mean, so the resolvability was likely not the cause of the different depths.

Therefore, we predict that the difference in interpreted depths was due to changing snow properties between the observations or from the accuracy in the radar interpretations. Future studies with data collection on the same day, and ideally time, between the systems will continue improving the validation of this airborne radar systems as it will reduce the uncertainties caused by temporal snow property changes (which impact the real permittivity). Due to logistics, our 2023 airborne radar was not able to be flown concurrently with the surface GPR data collection.

4.3 Near surface meltwater

The real permittivity for each hyperbolic analysis depth was higher than the density-derived estimates. For the 1 m probe depth, the hyperbolic analysis resulted in a real permittivity of $\epsilon' = 3.52 \pm 0.09$, higher than ice ($\epsilon' \sim 3.15$) (Section 3.2.2). We predict that the differences between real permittivity measurements and values higher than ice were due to near-surface meltwater. This near-surface meltwater also impacted the amount of interpretable airborne radar data in 2023.

We observed a drop in the real permittivity from the hyperbolic analysis surveys when the probe depth increased, indicative of near surface meltwater. The 1 and 1.5 m surveys were taken within minutes of each other so changes in snow properties between the measurements were not the cause for the drop in real permittivity. For the 1.5 m deep probe, we predict that there was drier snow below the top one meter which reduced the impact of the near surface meltwater on the bulk permittivity. Thawing by radiation does not extend deeper than 50-75 cm into the snow pack (Sharp, 1951), which supports a hypothesis of drier snow deeper in the snow column. As the extremely warm temperatures in 2023 were observed for a limited period, not enough melt water might have been generated to uniformly saturate the snow column.

For our study, we assumed a dry snow column for our real permittivity as we did not have sufficient data to determine the full snow column wetness across the region of study. Additionally, the snow depths from both the airborne radar and surface GPR when using a dry snow real permittivity were similar to

the probe depth for the last summer surface (Sections 3.1.3 and 3.2.2). Assuming the full snow column was dry will lead to an overestimation of depth if there is near surface meltwater. For example, using a snow density of 438 kg m^{-3}, water content increasing from 0 to 10% will decrease the velocity from 0.2 to 0.16 m ns^{-1} (ϵ' = 2.25 to 3.52) (Bradford and others, 2009). Near the 2023 Seward cores, by assuming the full snow column was dry, we overestimated the snow depth by ∼0.3 m (0.13 m w.e.). This calculated overestimation assumed dry snow underneath the top 1.5 m of wet snow with a real permittivity observed by the hyperbolic analysis. The possible overestimation of depth is within the calculated uncertainties assuming a uniform dry snow column and real permittivity from empirical relationships of snow density (Fig. 7) and thus should not greatly impact the estimated winter mass balances. However, including a more robust wet snow estimate would further refine the uncertainty analysis. We achieved some constraints on where the snow was wet from Sentinel 1 reflectivity and temperature lapse rates, however, the amount of liquid water content in the full snow column was still uncertain, so we did not include snow wetness in our calculated uncertainties.

Furthermore, we hypothesize that the initiation of melt prior to the 2023 airborne data acquisition caused a lower percentage of successful snow depth measurements due to attenuation of the radar in wetter snow. This was especially apparent on the Seward Glacier where interpretable reflectors were sparse for survey lines below ∼1600 m a.s.l. Lower elevations are more likely to be impacted by meltwater due to warmer temperatures. This was especially relevant for the 2018 and 2023 surveys which occurred in late May and thus experienced higher temperatures than in early May (Table 3, Figs. S14, S15). As seen on the Hubbard Glacier, the earlier survey dates in 2021 supported data retrieval to lower surface elevations than either the 2018 or 2023 surveys. Additional evidence of water impacting where the airborne radar interpretations were possible is that the upper Kaskawulsh data (Fig. 14) in 2023 had a much more prominent last summer surface than the Seward data (Fig. 3). This could be due to drier snow above the last summer surface on the upper Kaskawulsh, compared to area near the Seward core sites, which provides a stronger contrast between the dry winter snow and the last summer surface and thus a clearer reflector.

The Sentinel 1 reflectivity had yet to decrease at the higher elevation Kaskawulsh core location during the 2023 data acquisition compared to the Seward core location, implying drier snow on the Kaskawulsh (Fig. S18) (Section 3.3.2). The returned airborne radar amplitude from the last summer surface interpretations in 2023 data were also higher for the upper Kaskawulsh than near the Seward core sites (Fig.

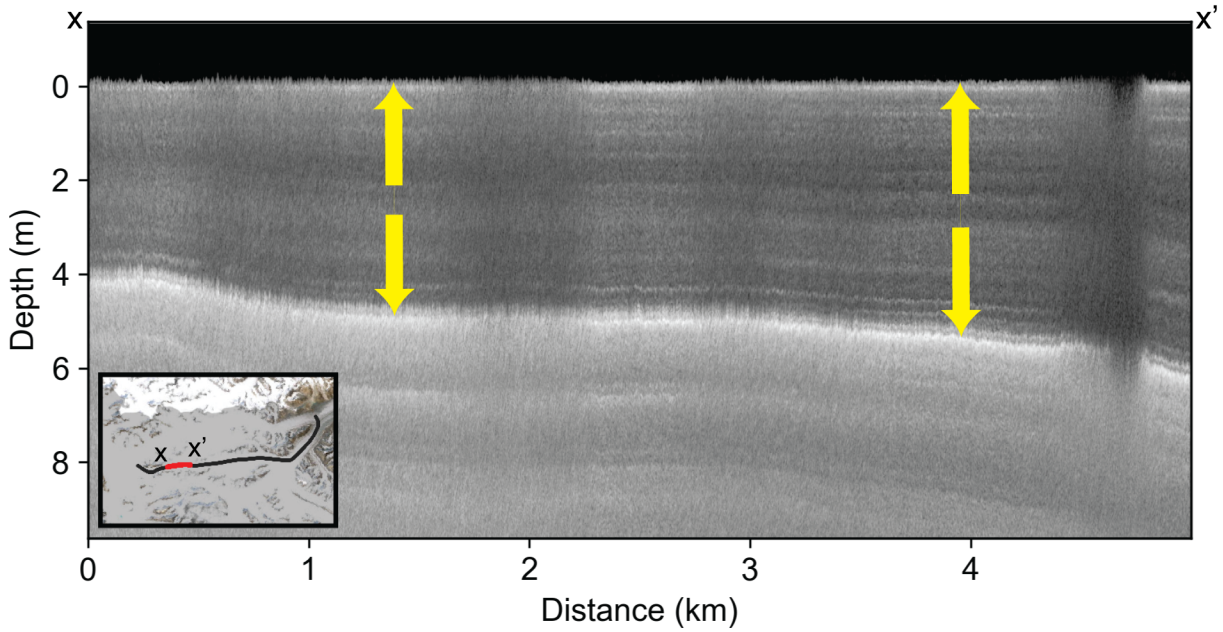

Fig. 14. Sample radargram from 2023 on the center arm of the Kaskawulsh Glacier with the extent of the inset box being the same as the inset in Fig. 4d. Radargram surface elevation was ~2700 m a.s.l. In the inset we include the path of the radargram in Fig. 4 as the black line, while this radargram is the red section. The radargram is flattened so that the surface is at zero depth and is read from x to x'.

S19c). Increased snow depth and survey altitude will also reduce the returned radar power from the last summer surface. However, there were similar interpreted snow depths between the upper Kaskawulsh and Seward glaciers, and the upper Kaskawulsh had a higher survey altitude. Therefore, it is more likely that the higher returned amplitude on the upper Kaskawulsh for the last summer surface was due to lower loss in the snow column. Our assumption of the dry snow column for calculating the real permittivity will result in an overestimation of depths at low elevations where melt has occurred, but shouldn't impact the dry, high elevation areas.

Due to the extreme topography in the St. Elias Mountains, the timing of future data acquisition should be carefully considered as lower elevations need earlier survey dates. Future studies, especially those with large spatial scale (Holt and others, 2024) should further explore and utilize historic Sentinel 1 reflectivity data to estimate surface snow wetness before and during planned data acquisition. This may require surveys to begin before the end of the accumulation period to better capture spatial patterns instead of attempting to fully measure the maximum depth of snow, which might result in data gaps. Such efforts should also obtain more constraints on snow wetness through: direct measurements of water content, a combination of snow density and hyperbolic analysis, radar wave velocity methods such as wide angle reflection and

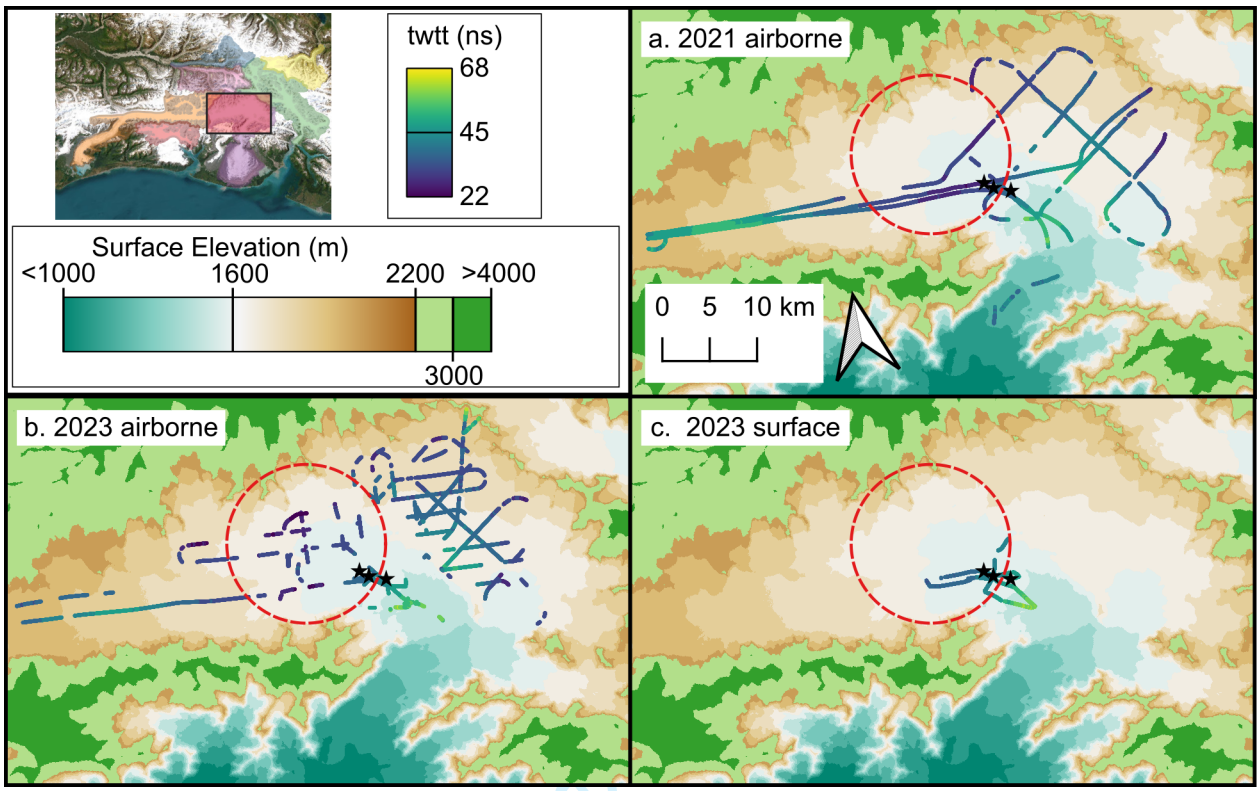

Fig. 15. Two-way travel times to the last summer surface on the Seward Glacier for the (a) 2021 and (b) 2023 airborne radar data, in addition to the (c) surface GPR data. To emphasize the 1000–2200 m elevation range, the Copernicus GLO-30 DEM background uses discrete steps of 100 m between 1000–2200 m, with single colors for 2200-3000 m and >3000 m. The three pit sites from 2023 are marked by black stars.

refraction or common mid-point, or developing melt models to retrieve snow column liquid water content.

4.4 Orographic shadowing

A major feature of interest was identified on the Seward Glacier which shows a spatially limited decrease of two-way travel times with increasing elevation along the main trunk of the glacier. The red circle in Fig. 15 shows the general area of decreased two-way travel time to the last summer surface, up to ∼15 ns (∼30%) quicker in this area than at the Seward throat and the Seward-Bering ice divide. This feature was apparent in all three Seward radar datasets. Areas of lower two-way travel time are also visible in the northeast and east edges of the Seward accumulation area.

In our work we assume that this decrease in two-way travel time is due to shallower snow depths in the region of the red circle (Fig. 15). However, two key snow properties, liquid water content and density, will also impact the radar wave speed and thus the two-way travel time (Section 2.2.3, 3.2.3). Here we asses whether the red circle marks a region of decreased snow depth, or changes in the liquid water content or

density. For this assessment, we assumed that the snow depth did not decrease across the red circle and would be the same depth as at the Seward throat and the Seward-Bering ice divide.

The first possible explanation is spatial variability in liquid water content across the Seward glacier. However, this is unlikely, as it would require increased liquid water content at both higher and lower surface elevations compared to the area of the red circle (Fig. 15). A decrease in liquid water at mid-elevations compared to higher elevations during the initiation of melt is not probable based on temperature patterns and the area of interest was not shadowed from solar radiation. Additionally, assuming the snow in the red circle was completely dry, the liquid water content at the Seward throat and Seward-Bering ice divide would need to be as high as ∼13%. Based on the 1 to 1.5 m snow wetness constraints from the 2023 pits, the snow in the mid-glacier was not completely dry (Section 3.2.2) and would thus require that higher and lower surface elevations to have liquid water content exceeding ∼13%. Furthermore, 13% liquid water content exceeds the maximum value of ∼10% used in studies investigating the impact of liquid water on radar (Lundberg and Thunehed, 2000; Bradford and others, 2009), potentially meaning higher liquid water content is unlikely to be encountered. Lastly, this feature was also observed in 2021, prior to significant melt, which further implies the decrease in two-way travel time is not caused by liquid water changes.

The second possible explanation, variability in snow density, is also unlikely to explain the quicker two-way travel times in the red circle. For there to not be a decrease in snow depth in the red circle, based on the equations from Sugiyama and others (2010), the snow density would need to be ∼200 kg m^{-3} in this region (Fig. 15) and 1000 kg m^{-3} elsewhere. Not only will seasonal snow not reach a density of 1000 kg m^{-3}, as this exceeds the density of ice, 200 kg m^{-3} is less than half of the observed density in the 2023 Seward cores.

We therefore hypothesize that the decrease in snow depth emphasized by the red circle in Fig. 15 was primarily due to an orographic precipitation shadow, causing this area to receive less snowfall than elsewhere along the center line of the Seward Glacier. High mountains >3000 m a.s.l. directly south of the red area in Fig. 15 are more than 1000 m higher than the accumulation area, possibly blocking storms. Parts of the upper Kaskawulsh appear to also experience both orographic enhancement and shadowing (Fig. 6). The strong reflector observed in Fig. 14 has a depth that increased by ∼50% in 5 km. As this change in two-way travel time is similar to the Seward Glacier changes in the orographic shadow, the changes in depth on the Kaskawulsh Glacier are also likely due to variable snow depth. These significant changes in snow depth in a few kilometers also support that the snow depth changed between the 2018

airborne radar data and the Kaskawulsh core, rather than changes in snow density. These short distance, kilometer-scale, variabilities in snow depth should be considered when planning future in situ and airborne surveys.

5 CONCLUSION

Airborne surveys combined with spatial limited in situ measurements provide a mechanism for regional assessment of winter mass balance SWE and mass of water in the St. Elias Mountains. In situ measurements are best used as validation of seasonal snow depths and providing critical density measurements to improve the accuracy of snow depth and SWE conversions. Glaciers in more maritime glaciers, such as Yahtse, Bering, Hubbard, and Seward were calculated to have significantly higher input masses than more inland glaciers such as Kaskawulsh, Walsh, and Logan. Hubbard had the highest input mass in our study. Based on our sensitivity test that used Mt. Logan core data, airborne surveys should focus on sampling the large regions of the accumulation areas rather than ensuring measurements reach the top of glaciers. A seasonal snow density of 438 ± 22 kg m^{-3} and a real permittivity of 1.86 ± 0.12, derived from in situ measurements on the Seward and Kaskawulsh glaciers agree well with values from more intensively studied Alaskan glaciers such as Wolverine and Gulkana. Additional in situ measurements should be undertaken in the future to further validate the real permittivity and snow density across this large and topographically varied region. Future work involving large-scale studies should consider using Sentinel 1 imagery for planning the timing of surveys to identify when the target areas began to experience large scale melting. Additionally, future work will also benefit from an increase in snow wetness measurements for the seasonal snowpack through in situ measurements and/or modeling of liquid water content.

6 DATA AVAILABILITY STATEMENT

The processed airborne data is retrievable from the CReSIS data archive for 2018 (`https://data.cresis.ku.edu/data/snow/2018_Alaska_SO/`), 2021 (`https://data.cresis.ku.edu/data/snow/2021_Alaska_SO/`), and 2023 (`https://data.cresis.ku.edu/data/snow/2023_Alaska_Cessna206/`).

All other data, radar interpretations, and code are available on reDATA. The dataset is available at `https://figshare.com/s/2683591e0397f3c56f8b` during the review process. After the article is accepted, it will be available at `https://doi.org/10.25422/azu.data.29473529`.

7 SUPPLEMENTARY MATERIAL

The supplementary material as a single PDF for this article can be found at `https://github.com/danielmf-1729/StEliasSnowRadar.git`.

8 ACKNOWLEDGMENTS

We would like to thank Victor Devaux-Chupin and Annegret Pohle from the Geophysical Institute at the University of Alaska Fairbanks for their help with the 2023 Seward data collection. Michael Daniel (MD), John Holt (JH), Douglas Brinkerhoff (DB), and Martin Truffer (MT) were supported by NSF award 1929566. This NSF award also supported the collection of the 2023 data. MD was further supported by NASA award 80NSSC24K1463. Mikaila Mannello (MM) was supported by the University of Maine Bob and Judy Sturgis Exploration Fund and the University of Maine Graduate Student Government. Jilu Li (JL) and Fernando Rodriguez-Morales (FRM) were supported by the Center for Remote Sensing and Integrated Systems (CReSIS).

9 AUTHOR CONTRIBUTIONS

MD, MM, DB, and MT collected the 2023 surface GPR data and snow cores. JH and FRM collected the 2023 airborne radar data. JL processed the 2023 airborne radar data. MM advised on surface GPR data processing and interpretation. MD primarily performed all data interpretations and analysis, as well as wrote the original draft. All authors contributed to editing and review.

REFERENCES

ASF DAAC (2024) Contains modified Copernicus Sentinel data 2017-2023, processed by ESA

Beaudoin-Galaise M and Jutras S (2022) Comparison of manual snow water equivalent (SWE) measurements: seeking the reference for a true SWE value in a boreal biome. *The Cryosphere*, **16**(8), 3199–3214, ISSN 1994-0424 (doi: 10.5194/tc-16-3199-2022)

Bradford JH, Harper JT and Brown J (2009) Complex dielectric permittivity measurements from ground-penetrating radar data to estimate snow liquid water content in the pendular regime: MEASURING SWE WITH GPR. *Water Resources Research*, **45**(8), ISSN 00431397 (doi: 10.1029/2008WR007341)

Brinkerhoff DJ, Tober BS, Daniel M, Devaux-Chupin V, Christoffersen MS, Holt JW, Larsen CF, Fahnestock M, Loso MG, Timm KMF, Mitchell RC and Truffer M (2025) The demise of the world's largest piedmont glacier: a probabilistic forecast. *The Cryosphere*, **19**(6), 2321–2353, ISSN 1994-0424 (doi: 10.5194/tc-19-2321-2025)

Cogley J, Hock R, Rasmussen L, Arendt A, Bauder A, Braithwaite R, Jansson P, Kaser G, Möller M, Nicholson L and Zemp M (2011) *Glossary of Glacier Mass Balance and Related Terms*, volume IHP-VII Technical Documents in Hydrology No. 86, IACS Contribution No. 2. UNESCO-IHP, Paris

Cuffey KM and Paterson WSB (2010) *The physics of glaciers*. Butterworth-Heineman, Amsterdam Heidelberg, 4. ed edition, ISBN 978-0-12-369461-4

Dozier J, Bair EH and Davis RE (2016) Estimating the spatial distribution of snow water equivalent in the world's mountains. *WIREs Water*, **3**(3), 461–474, ISSN 2049-1948, 2049-1948 (doi: 10.1002/wat2.1140)

Fisher DA, Wake C, Kreutz K, Yalcin K, Steig E, Mayewski P, Anderson L, Zheng J, Rupper S, Zdanowicz C, Demuth M, Waszkiewicz M, Dahl-Jensen D, Goto-Azuma K, Bourgeois JB, Koerner RM, Sekerka J, Osterberg E, Abbott MB, Finney BP and Burns SJ (2006) Stable Isotope Records from Mount Logan, Eclipse Ice Cores and Nearby Jellybean Lake. Water Cycle of the North Pacific Over 2000 Years and Over Five Vertical Kilometres: Sudden Shifts and Tropical Connections. *Géographie physique et Quaternaire*, **58**(2-3), 337–352, ISSN 1492-143X, 0705-7199 (doi: 10.7202/013147ar)

Gagliano E, Shean D, Henderson S and Vanderwilt S (2023) Capturing the Onset of Mountain Snowmelt Runoff Using Satellite Synthetic Aperture Radar. *Geophysical Research Letters*, **50**(21), e2023GL105303, ISSN 0094-8276, 1944-8007 (doi: 10.1029/2023GL105303)

Gusmeroli A, Wolken GJ and Arendt AA (2014) Helicopter-borne radar imaging of snow cover on and around glaciers in Alaska. *Annals of Glaciology*, **55**(67), 78–88, ISSN 0260-3055, 1727-5644 (doi: 10.3189/2014AoG67A029)

Holt JW, Andrews LC, MacGregor JA, Aschwanden A, Behrangi A, Campbell SW, Daniel MF, Enderlin EM, Fahnestock MA, Felikson D, Florentine C, Flowers GE, Harig CT, Larsen CF, Leuschen CJ, Morlighem M, O'Neel S, Robinson K, Rounce DR, Studinger M, Tober BS and Truffer M (2024) Snow4Flow: Concept Paper for a NASA Earth Venture Suborbital-4 Investigation (doi: 10.5281/ZENODO.15985778), version Number: 2

Hugonnet R, McNabb R, Berthier E, Menounos B, Nuth C, Girod L, Farinotti D, Huss M, Dussaillant I, Brun F and Kääb A (2021) Accelerated global glacier mass loss in the early twenty-first century. *Nature*, **592**(7856), 726–731, ISSN 0028-0836, 1476-4687 (doi: 10.1038/s41586-021-03436-z)

Kellndorfer J, Cartus O, Lavalle M, Magnard C, Milillo P, Oveisgharan S, Osmanoglu B, Rosen PA and Wegmüller U (2022) Global seasonal Sentinel-1 interferometric coherence and backscatter data set. *Scientific Data*, **9**(1), 73, ISSN 2052-4463 (doi: 10.1038/s41597-022-01189-6)

Knight R, Tercier P and Irving J (2004) The effect of vertical measurement resolution on the correlation structure of a ground penetrating radar reflection image. *Geophysical Research Letters*, **31**(21), 2004GL021112, ISSN 0094-8276, 1944-8007 (doi: 10.1029/2004GL021112)

Larsen CF, Burgess E, Arendt AA, O'Neel S, Johnson AJ and Kienholz C (2015) Surface melt dominates Alaska glacier mass balance: Alaska Glacier Mass Balance. *Geophysical Research Letters*, **42**(14), 5902–5908, ISSN 00948276 (doi: 10.1002/2015GL064349)

Li J, Rodriguez-Morales F, Arnold E, Leuschen C, Paden J, Shang J, Gomez-Garcia D and Larsen C (2019) Airborne Snow Measurements Over Alaska Mountains and Glaciers With A Compact FMCW Radar. In *IGARSS 2019 - 2019 IEEE International Geoscience and Remote Sensing Symposium*, 3966–3969, IEEE, Yokohama, Japan, ISBN 978-1-5386-9154-0 (doi: 10.1109/IGARSS.2019.8900034)

Li J, Rodriguez-Morales F, Fettweis X, Ibikunle O, Leuschen C, Paden J, Gomez-Garcia D and Arnold E (2023) Snow stratigraphy observations from Operation IceBridge surveys in Alaska using S and C band airborne ultra-wideband FMCW (frequency-modulated continuous wave) radar. *The Cryosphere*, **17**(1), 175–193, ISSN 1994-0424 (doi: 10.5194/tc-17-175-2023)

Lundberg A and Thunehed H (2000) Snow Wetness Influence on Impulse Radar Snow Surveys Theoretical and Laboratory Study. *Hydrology Research*, **31**(2), 89–106, ISSN 0029-1277, 2224-7955 (doi: 10.2166/nh.2000.0007)

MacGregor JA, Boisvert LN, Medley B, Petty AA, Harbeck JP, Bell RE, Blair JB, Blanchard-Wrigglesworth E, Buckley EM, Christoffersen MS, Cochran JR, Csathó BM, Marco EL, Dominguez RT, Fahnestock MA, Farrell SL, Gogineni SP, Greenbaum JS, Hansen CM, Hofton MA, Holt JW, Jezek KC, Koenig LS, Kurtz NT, Kwok R, Larsen CF, Leuschen CJ, Locke CD, Manizade SS, Martin S, Neumann TA, Nowicki SM, Paden JD, Richter-Menge JA, Rignot EJ, Rodríguez-Morales F, Siegfried MR, Smith BE, Sonntag JG, Studinger M, Tinto KJ, Truffer M, Wagner TP, Woods JE, Young DA and Yungel JK (2021) The Scientific Legacy of NASA's Operation IceBridge. *Reviews of Geophysics*, **59**(2), ISSN 8755-1209, 1944-9208 (doi: 10.1029/2020RG000712)

Marcus MG and Ragle RH (1970) Snow Accumulation in the Icefield Ranges, St. Elias Mountains, Yukon. *Arctic and Alpine Research*, **2**(4), 277, ISSN 00040851 (doi: 10.2307/1550241)

McGrath D, Sass L, O'Neel S, Arendt A, Wolken G, Gusmeroli A, Kienholz C and McNeil C (2015) End-of-winter snow depth variability on glaciers in Alaska. *Journal of Geophysical Research: Earth Surface*, **120**(8), 1530–1550, ISSN 21699003 (doi: 10.1002/2015JF003539)

McGrath D, Sass L, O'Neel S, McNeil C, Candela SG, Baker EH and Marshall HP (2018) Interannual snow accumulation variability on glaciers derived from repeat, spatially extensive ground-penetrating radar surveys. *The Cryosphere*, **12**(11), 3617–3633, ISSN 1994-0424 (doi: 10.5194/tc-12-3617-2018)

Millan R, Mouginot J, Rabatel A and Morlighem M (2022) Ice velocity and thickness of the world's glaciers. *Nature Geoscience*, **15**(2), 124–129, ISSN 1752-0894, 1752-0908 (doi: 10.1038/s41561-021-00885-z)

Nagler T, Rott H, Ripper E, Bippus G and Hetzenecker M (2016) Advancements for Snowmelt Monitoring by Means of Sentinel-1 SAR. *Remote Sensing*, **8**(4), 348, ISSN 2072-4292 (doi: 10.3390/rs8040348)

National Weather Service (2024) Yakutat

Ni SH, Huang YH, Lo KF and Lin DC (2010) Buried pipe detection by ground penetrating radar using the discrete wavelet transform. *Computers and Geotechnics*, **37**(4), 440–448, ISSN 0266352X (doi: 10.1016/j.compgeo.2010.01.003)

Ochwat NE, Marshall SJ, Moorman BJ, Criscitiello AS and Copland L (2021) Evolution of the firn pack of Kaskawulsh Glacier, Yukon: meltwater effects, densification, and the development of a perennial firn aquifer. *The Cryosphere*, **15**(4), 2021–2040, ISSN 1994-0424 (doi: 10.5194/tc-15-2021-2021)

OpenTopography (2021) Copernicus GLO-90 Digital Surface Model (doi: 10.5069/G9028PQB)

Paden J, Li J, Leuschen C, Rodgriguez-Morales F and Hale R (2014) IceBridge Snow Radar L1B Geolocated Radar Echo Strength Profiles, Version 2 (doi: 10.5067/FAZTWP500V70)

Proksch M, Rutter N, Fierz C and Schneebeli M (2016) Intercomparison of snow density measurements: bias, precision, and vertical resolution. *The Cryosphere*, **10**(1), 371–384, ISSN 1994-0424 (doi: 10.5194/tc-10-371-2016)

RGI Consortium (2023) Randolph Glacier Inventory - A Dataset of Global Glacier Outlines, Version 7 (doi: 10.5067/F6JMOVY5NAVZ)

Robinson KM, Flowers GE and Rounce DR (2025) Sensitivity of modelled mass balance and runoff to representations of debris and accumulation on the Kaskawulsh Glacier, Yukon, Canada. *Journal of Glaciology*, **71**, e42, ISSN 0022-1430, 1727-5652 (doi: 10.1017/jog.2025.8)

Rodriguez-Morales F, Li J, Alvestegui DGG, Shang J, Arnold EJ, Leuschen CJ, Larsen CF, Shepherd A, Hvidegaard SM and Forsberg R (2021) A Compact, Reconfigurable, Multi-UWB Radar for Snow Thickness Evaluation and Altimetry: Development and Field Trials. *IEEE Journal of Selected Topics in Applied Earth Observations and Remote Sensing*, **14**, 6755–6765, ISSN 1939-1404, 2151-1535 (doi: 10.1109/JSTARS.2021.3092313)

Rott H and Nagler T (1993) CAPABILITIES OF ERS-1 SAR FOR SNOW AND GLACIER MONITORING IN ALPINE AREAS. In *Second ERS-1 Sumposium - Space at the Service of our Environment*, Hamburg, Germany

Rounce DR, Hock R, Maussion F, Hugonnet R, Kochtitzky W, Huss M, Berthier E, Brinkerhoff D, Compagno L, Copland L, Farinotti D, Menounos B and McNabb RW (2023) Global glacier change in the 21st century: Every

increase in temperature matters. *Science*, **379**(6627), 78–83, ISSN 0036-8075, 1095-9203 (doi: 10.1126/science.abo1324)

Sharp RP (1951) Features of the Firn on Upper Seward Glacier St. Elias Mountains, Canada. *The Journal of Geology*, **59**(6), 599–621, ISSN 0022-1376, 1537-5269 (doi: 10.1086/625915)

Sihvola A and Tiuri M (1986) Snow Fork for Field Determination of the Density and Wetness Profiles of a Snow Pack. *IEEE Transactions on Geoscience and Remote Sensing*, **GE-24**(5), 717–721, ISSN 0196-2892 (doi: 10.1109/TGRS.1986.289619)

Sugiyama S, Enomoto H, Fujita S, Fukui K, Nakazawa F and Holmlund P (2010) Dielectric permittivity of snow measured along the route traversed in the Japanese–Swedish Antarctic Expedition 2007/08. *Annals of Glaciology*, **51**(55), 9–15, ISSN 0260-3055, 1727-5644 (doi: 10.3189/172756410791392745)

Tober B S and Christoffersen M (2023) btobers/RAGU: RAGU is pypi installable (doi: 10.5281/ZENODO.10182874)

Tober BS, Holt JW, Christoffersen MS, Truffer M, Larsen CF, Brinkerhoff DJ and Mooneyham SA (2023) Comprehensive Radar Mapping of Malaspina Glacier (Sít' Tlein), Alaska—The World's Largest Piedmont Glacier—Reveals Potential for Instability. *Journal of Geophysical Research: Earth Surface*, **128**(3), e2022JF006898, ISSN 2169-9003, 2169-9011 (doi: 10.1029/2022JF006898)

Torres R, Snoeij P, Geudtner D, Bibby D, Davidson M, Attema E, Potin P, Rommen B, Floury N, Brown M, Traver IN, Deghaye P, Duesmann B, Rosich B, Miranda N, Bruno C, L'Abbate M, Croci R, Pietropaolo A, Huchler M and Rostan F (2012) GMES Sentinel-1 mission. *Remote Sensing of Environment*, **120**, 9–24, ISSN 00344257 (doi: 10.1016/j.rse.2011.05.028)

Trabant DC, Krimmel RM and Post A (1991) A preliminary forecast of the advance of Hubbard Glacier and its influence on Russell Fiord, Alaska. *Water-Resources Investigations Report*, **90-4172** (doi: 10.3133/wri904172)

Trabant DC, Krimmel RM, Echelmeyer KA, Zirnheld SL and Elsberg DH (2003) The slow advance of a calving glacier: Hubbard Glacier, Alaska, U.S.A. *Annals of Glaciology*, **36**, 45–50, ISSN 0260-3055, 1727-5644 (doi: 10.3189/172756403781816400)

Turbé C, Karbou F, Rabatel A and Gouttevin I (2024a) Snowmelt Dynamics in a Temperate Glacier Using Sentinel-1 SAR Images: A Case Study on Saint-Sorlin Glacier, French Alps. *IEEE Journal of Selected Topics in Applied Earth Observations and Remote Sensing*, **17**, 8904–8917, ISSN 1939-1404, 2151-1535 (doi: 10.1109/JSTARS.2024.3384030)

Turbé C, Karbou F, Rabatel A, Gouttevin I and Racoviteanu A (2024b) On the Use of Sentinel-1 to Study Snow Melt Dynamics in a Glacierized Mountain Catchment. In *IGARSS 2024 - 2024 IEEE International Geoscience and*

Remote Sensing Symposium, 1833–1837, IEEE, Athens, Greece, ISBN 9798350360325 (doi: 10.1109/IGARSS53475.2024.10642901)

US Department of Agriculture NRCS National Water and Climate Center (2025) Snow and Climate Monitoring Predefined Reports and Maps

Western Regional Climate Center (2024) Tana Knob Alaska

Windnagel A, Hock R, Maussion F, Paul F, Rastner P, Raup B and Zemp M (2023) Which glaciers are the largest in the world? *Journal of Glaciology*, **69**(274), 301–310, ISSN 0022-1430, 1727-5652 (doi: 10.1017/jog.2022.61)

Winski D, Osterberg E, Ferris D, Kreutz K, Wake C, Campbell S, Hawley R, Roy S, Birkel S, Introne D and Handley M (2017) Industrial-age doubling of snow accumulation in the Alaska Range linked to tropical ocean warming. *Scientific Reports*, **7**(1), 17869, ISSN 2045-2322 (doi: 10.1038/s41598-017-18022-5)

Wu Z and Liu S (2012) Imaging the debris internal structure and estimating the effect of debris layer on ablation of Glacier ice. *Journal of the Geological Society of India*, **80**(6), 825–835, ISSN 0016-7622, 0974-6889 (doi: 10.1007/s12594-012-0211-z)

Young EM, Flowers GE, Berthier E and Latto R (2021) An imbalancing act: the delayed dynamic response of the Kaskawulsh Glacier to sustained mass loss. *Journal of Glaciology*, **67**(262), 313–330, ISSN 0022-1430, 1727-5652 (doi: 10.1017/jog.2020.107)

Zeller L, McGrath D, Sass L, O'Neel S, McNeil C and Baker E (2022) Beyond glacier-wide mass balances: parsing seasonal elevation change into spatially resolved patterns of accumulation and ablation at Wolverine Glacier, Alaska. *Journal of Glaciology*, 1–16, ISSN 0022-1430, 1727-5652 (doi: 10.1017/jog.2022.46)